

# Transport of Molecules through and on Carbon Nanostructures

by  
Lee William Drahushuk

Bachelor of Science in Chemical Engineering  
Cornell University, 2010

SUBMITTED TO THE DEPARTMENT OF CHEMICAL ENGINEERING IN  
PARTIAL FULFILLMENT OF THE REQUIREMENTS FOR THE DEGREE OF

DOCTOR OF PHILOSOPHY IN CHEMICAL ENGINEERING  
AT THE  
MASSACHUSETTS INSTITUTE OF TECHNOLOGY

NOVEMBER 2017

[February 2018]

© Massachusetts Institute of Technology 2017. All rights reserved

The author hereby grants to MIT permission to reproduce  
and to distribute publicly paper and electronic  
copies of this thesis document in whole or in part  
in any medium now known or hereafter created.

Signature of Author:

Signature redacted

Department of Chemical Engineering  
Nov, 2017

Certified by:

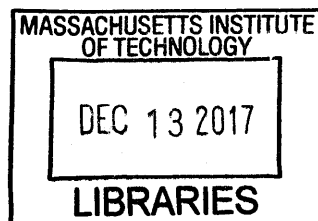
Signature redacted

Michael S. Strano  
Carbon P. Dubbs Professor of Chemical Engineering  
Thesis Supervisor

Accepted by:

Signature redacted

Patrick S. Doyle  
Robert T. Haslam Professor of Chemical Engineering  
Chairman, Committee for Graduate Students



ARCHIVES



# Transport of Molecules through and on Carbon Nanostructures

by  
Lee William Drahushuk

Submitted to the Department of Chemical Engineering  
on November 20, 2017 in Partial fulfillment of the  
requirements for the Degree of Doctor of Philosophy in  
Chemical Engineering

## Abstract

Single-layer graphene membranes and other 2D membranes can realize very high gas permeation fluxes due to their atomic or unit cell thickness. Established modeling approaches for membrane transport consider transport through a finite and continuum thickness, and therefore they do not apply to the emerging field of 2D membranes, motivating the development of new theoretical treatments. In this thesis, I first developed an analytical theory for the transport of gases through single-layer graphene membranes, from the perspective of using pores in the graphene layer as a means for separation. I considered two pathways for the transport. The first being direct gas phase impingement on the pore, for which the large-pore separation factors are dictated by Knudsen selectivity, inversely proportional to the molecular weight; selectivity exceeding Knudsen is possible with smaller pores that reach a size commensurate with the size of the molecule, enabling separation by molecular sieving. The second pathway involves adsorption and transport on the graphene surface, similar to mechanisms in heterogeneous catalysis, which becomes more relevant for larger, strongly-adsorbing molecules. These models and pathways are applied for an estimate of a  $N_2/H_2$  separation and as an explanation for results observed in the molecular dynamics literature.

I applied our understanding of nanopore mechanisms and developed analysis of gas transport through graphene with approximately one selective nanopore etched into it, using experimental data from Bunch et al at Boston University for transport of He,  $H_2$ , Ne, Ar, and  $CO_2$  through a small area graphene membrane with a single or few pores. The transport was measured by collaborators via monitoring the deflection of a graphene flake sealing a pressurized, 5  $\mu m$  diameter microcavity on the surface of a Si/SiO<sub>2</sub> wafer. For this experimental system, I report on a mathematical formalism that allows one to detect and analyze stochastic changes in the gas phase fluxes from graphene membranes, extracting activation energies of pore rearrangements, 1.0 eV, and even identifying contributions from multiple, isolated pores.

One opportunity that I identified is the use of a molecularly sized nanopore to ‘direct write’ the flux using a translatable platform. I performed an exploratory investigation of this concept of using a “nanonozzle,” a nanometer scale pore that can deliver a flow of

material locally, to grow nanoscale features. The model application was the growth of a graphene nanoribbon on a surface. I explored a variety of analytical mathematical models to understand the parameters and limitations of such a system. I developed a simple simulation of the nanoribbon growth and compared the results to the models for a range of parameters, considering the reasons for differences between the simulated and calculated results. This analysis provides considerations for the experimental design of such a system.

Overall, the theories in this thesis and the analysis in they enable should aid the development of 2D membranes for separations applications and a novel direct write method for nanoscale patterning.



## Acknowledgements

The completion of this thesis wouldn't have been possible without the support, advice, and encouragement of my thesis advisor, Professor Michael S. Strano. His enthusiasm and active engagement in research has helped drive forward my work whenever I needed it. His experience and direction has also allowed me to grow and learn how to focus the direction of and present my work to be most impactful. And though I met with them less frequently, my thesis committee members, Professor Daniel Blankshtein and Professor Richard Braatz, have been an important source of feedback, allowing me to improve the rigor and presentation of my work.

I'd like to thank my collaborators for the analysis of the experimental data on graphene membrane transports, Dr. Luda Wang and Professor J. Scott Bunch. While working in the Bunch lab, Dr. Wang collected the experimental data set on gas transport through graphene, and then allowed us the opportunity to work together in its analysis.

I have had the opportunity to work alongside and talk with many amazing students and postdocs while in the Strano research group. In particular some of the members to help me when starting were Nigel Reuel, Qing Hua Wang, Zhong Jin, Steven Shimizu, and Joel Abrahamson, and Geraldine Paulus. Over the course of the program, I've also had the opportunity to work more closely with Steven Shimizu, Kumar Varoon Agrawal, Jesse Benck, Ananth Govind Rajan, and Samuel Faucher. I also enjoyed going on the group camping trip with all the members who able to attend. Also, my time at MIT wouldn't have been what it was without my friends. I always looked forward to the chances to play board games friends in ChemE and Sid-Pac.

And finally, my mother, father, grandmother, aunts, and uncles, have been an important source of encouragement and support throughout my time in graduate school.

## CONTENTS

<b>1 INTRODUCTION TO GRAPHENE AND NANOSCALE TRANSPORT .....</b>	<b>8</b>
1.1 Graphene for 2D Membranes .....	8
1.2 Application of Nanoscale Transport to a Nanonozzle .....	17
<b>2 THEORY OF 2D MEMBRANE TRANSPORT.....</b>	<b>19</b>
2.1 Significance of 2D Membrane Theory .....	19
2.2 Results and Discussion.....	22
2.2.1 Gas phase pathway.....	24
2.2.2 Adsorbed phase pathway .....	26
2.2.3 Diffusion limited case.....	33
2.2.4 Model Pores .....	35
2.2.5 Model Parameters .....	36
2.2.6 Implications.....	40
2.3 Conclusions.....	42
<b>3 EXPERIMENTAL METHODS AND ANALYSIS OF STOCHASTIC GRAPHENE GAS TRANSPORT.....</b>	<b>43</b>
3.1 Introduction.....	43
3.2 Experimental Methods .....	45
3.3 Results and Discussion.....	46
3.3.1 Analysis of AFM Membrane Deflection Curves .....	46
3.3.2 A Mathematical Interpretation of Intersecting Deflection Curves .....	51
3.3.3 Hidden Markov Analysis of Time Dependent Permeance .....	55
3.3.4 Evaluation of Average Permeance in Relative to Expected Behavior.....	57
3.4 Conclusions.....	58
<b>4 ANALYSIS OF MULTIPLE STOCHASTIC STATES IN FINITE PORE SYSTEM .....</b>	<b>60</b>
4.1 Introduction.....	60
4.2 Assignment of system to discrete number of pores described by Markov Network.....	61
4.2.1 Three pore model .....	61
4.3 Comparison to simulated data sets.....	65
4.3.1 Simulation procedures .....	67
4.3.2 Analysis of Goodness of Fit of Data Sets .....	70

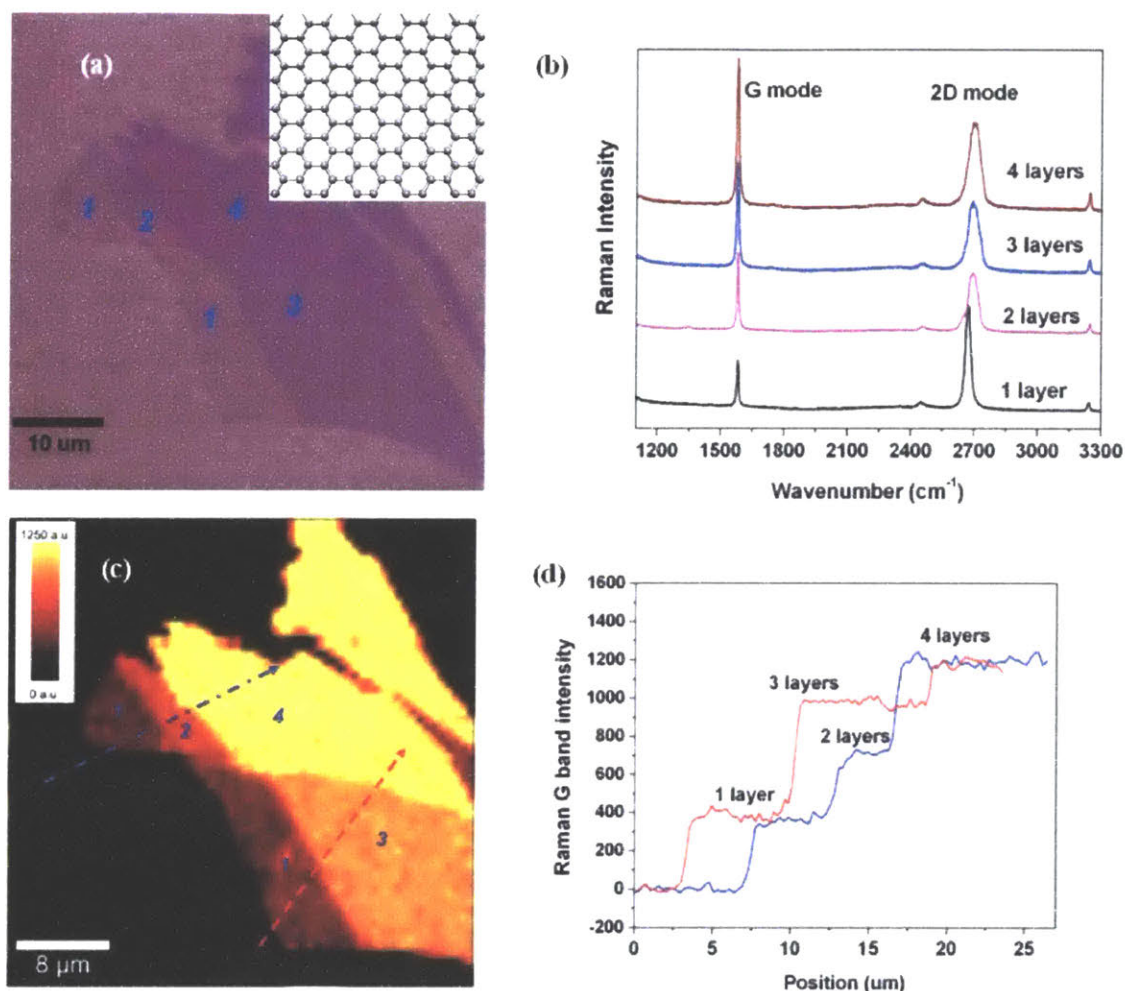
4.3.3	Mechanism for switching.....	75
<b>4.4</b>	<b>Conclusions.....</b>	<b>78</b>
<b>5</b>	<b>EXPLORATION OF DIRECT WRITE SYNTHESIS VIA A NANONOZZLE: FUNDAMENTAL SCALING LAWS .....</b>	<b>79</b>
<b>5.1</b>	<b>Significance of direct write nanoribbon synthesis .....</b>	<b>79</b>
<b>5.2</b>	<b>Simplified analytical models for describing ribbon growth from a nanonozzle</b>	<b>80</b>
5.2.1	1D toy model with diffusion, convection, and reaction.....	81
5.2.2	2D model with diffusion and reaction .....	83
<b>5.3</b>	<b>Models and Simulations in 3D .....</b>	<b>87</b>
5.3.1	Nanonozzle Simulations .....	88
5.3.2	Low Reaction Rate 3D Analytical Solution.....	90
5.3.3	Non-dimensional Notation.....	93
5.3.4	Comparison between 3D Model and Simulations .....	95
5.3.5	Towards Realizing an Experimental Nanonozzle System .....	100
<b>5.4</b>	<b>Conclusions and Outlook for Nanonozzle .....</b>	<b>102</b>
<b>6</b>	<b>CONCLUSIONS AND FUTURE APPLICATIONS.....</b>	<b>103</b>
<b>7</b>	<b>BIBLIOGRAPHY .....</b>	<b>107</b>

# 1 INTRODUCTION TO GRAPHENE AND NANOSCALE TRANSPORT

## 1.1 Graphene for 2D Membranes

Graphene is interesting because of its unique electronic properties, strong mechanical strength, and nanoscale dimensions.<sup>2, 3</sup> Single layer graphene consists of a monolayer of covalently bonded  $sp^2$  hybridized carbon atoms, depicted in the Figure 1a inset, in the conventional hexagonal planar array, creating a 2D electronic system. There is interest in using single layer graphene (SLG) and other graphene derivatives<sup>4</sup> as membranes for a variety of applications, including the membrane applications of interest here.

The two most relevant methods of obtaining graphene are mechanically exfoliation and chemical vapor deposition (CVD). Mechanical exfoliation, also commonly referred to as the “scotch-tape method,” is a process that typically uses repeated contact of a graphite flake with scotch tape; each successive contact with the tape separates pulls sheets of the flake apart from each other, resulting in a thinner and thinner flake.<sup>5</sup> After enough contacts, there are only a few layers in the spot on the tape, and it is pressed against a Si/SiO<sub>2</sub> surface to leave flakes of a range of thickness down to single layer. Single layer regions can be identified optically in a microscope, enabled by an interference effect, and confirmed by Raman spectroscopy, demonstrated in Figure 1.

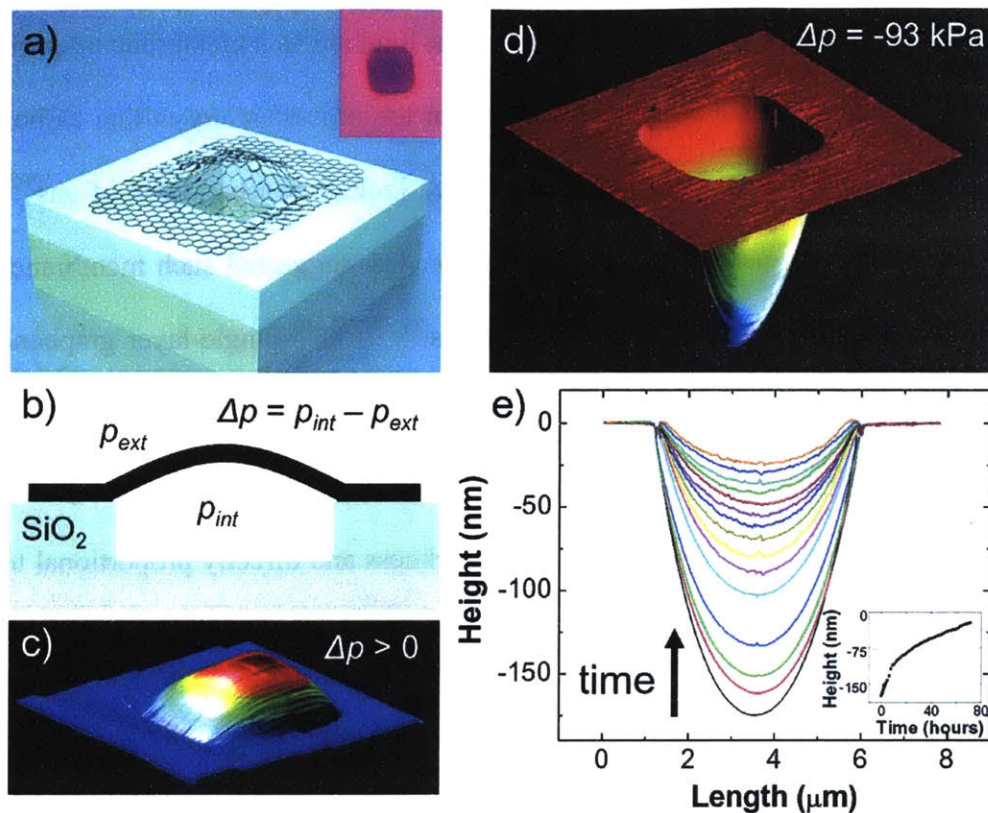


**Figure 1:** (a) Optical image of graphene with one, two, three, and four layers; (inset) illustration of graphene lattice, sp<sup>2</sup> hybridized carbon atoms. (b) Raman spectra as a function of number of layers. (c) Raman image plotted by the intensity of G band. (d) The cross section of Raman image, which corresponds to the dash lines. Adapted with permission from Ni, Z.H. *et al. Nano letters* 7, 2458-63 (2007). Copyright 2007 American Chemical Society.<sup>6</sup>

CVD synthesis is the other relevant source of graphene in research of single layer graphene membranes. In particular, CVD can produce large areas of graphene, with only practical limitations of furnace design, unlike the small areas produced by mechanical exfoliation. Graphene is most commonly grown on a copper foil substrate, but it can also

be grown on nickel as well as other, less commonly used substrates. The CVD process can be done at atmospheric pressure (with an inert diluent gas) or in vacuum, most often using methane as the carbon source, in the presence of hydrogen. Growth on copper substrates typically results in predominantly monolayer graphene. From there, the graphene can be transferred to an arbitrary substrate, usually by supporting the graphene with a polymer layer and etching away the copper.<sup>5</sup> Graphene produced from mechanical exfoliation usually has a fewer defects and grain boundaries compared to graphene grown by CVD processes, however, mechanical exfoliation is not scalable to large areas, therefore the advance of CVD graphene growth is an important part of the development of graphene membranes.

Pristine, single-layer graphene is impermeable to even the smallest of gases,<sup>7</sup> though recent work has shown there is a mechanism for proton transport.<sup>8</sup> The 2008 experiment in the McEuen group, depicted in Figure 2, used a transferred mechanically exfoliated graphene over a microchamber. After exposing the sample to a Helium pressurized (or vacuum) environment over the course of days, returning the sample to atmospheric conditions results in an upwards (or downwards) deflection of the graphene over the microchamber that is measurable with AFM. The deflection persists, slowly returning to zero over days with a rate consistent with diffusion of gases through the silicon oxide surface under the graphene, which shows that the He gas does leak from the microchamber through the graphene.



**Figure 2:** (a) Schematic of a graphene sealed microchamber. (Inset) optical image of a single atomic layer graphene drumhead on 440 nm of SiO<sub>2</sub>. The dimensions of the microchamber are 4.75 μm × 4.75 μm × 380 nm. (b) Side view schematic of the graphene sealed microchamber. (c) Tapping mode atomic force microscope (AFM) image of a ~ 9 nm thick many layer graphene drumhead with  $\Delta p > 0$ . The dimensions of the square microchamber are 4.75 μm × 4.75 μm. The upward deflection at the center of the membrane is  $z = 90$  nm. (d) AFM image of the graphene sealed microchamber of Figure 2a with  $\Delta p = -93$  kPa across it. The minimum dip in the  $z$  direction is 175 nm. (e) AFM line traces taken through the center of the graphene membrane of (a). The images were taken continuously over a span of 71.3 h and in ambient conditions. (Inset) deflection at the center of the graphene membrane vs time. The first deflection measurement ( $z = 175$  nm) is taken 40 min after removing the microchamber from vacuum. Reprinted with permission from Bunch, J.S. et al. *Nano letters* 8, 2458-62 (2008). Copyright 2008 American Chemical Society.<sup>7</sup>

Though pristine graphene is impermeable, it can function as a membrane after the layer is suitably treated to create atomic scale pores in the otherwise crystalline carbon lattice. A variety of simulations and calculations have looked at separations of gas<sup>9-23</sup> and liquid<sup>24-29</sup> systems. In particular, theoretical work has suggested such membranes could have large separation factors for gas separations.<sup>17, 18, 23, 30</sup> Single-layer graphene membranes differ fundamentally from typical bulk polymeric membranes. The basic model for polymeric membranes is constant permeability, with the flux,  $J$ , through the membrane inversely proportional to the membrane thickness and directly proportional to the driving pressure force,  $\Delta p$ .

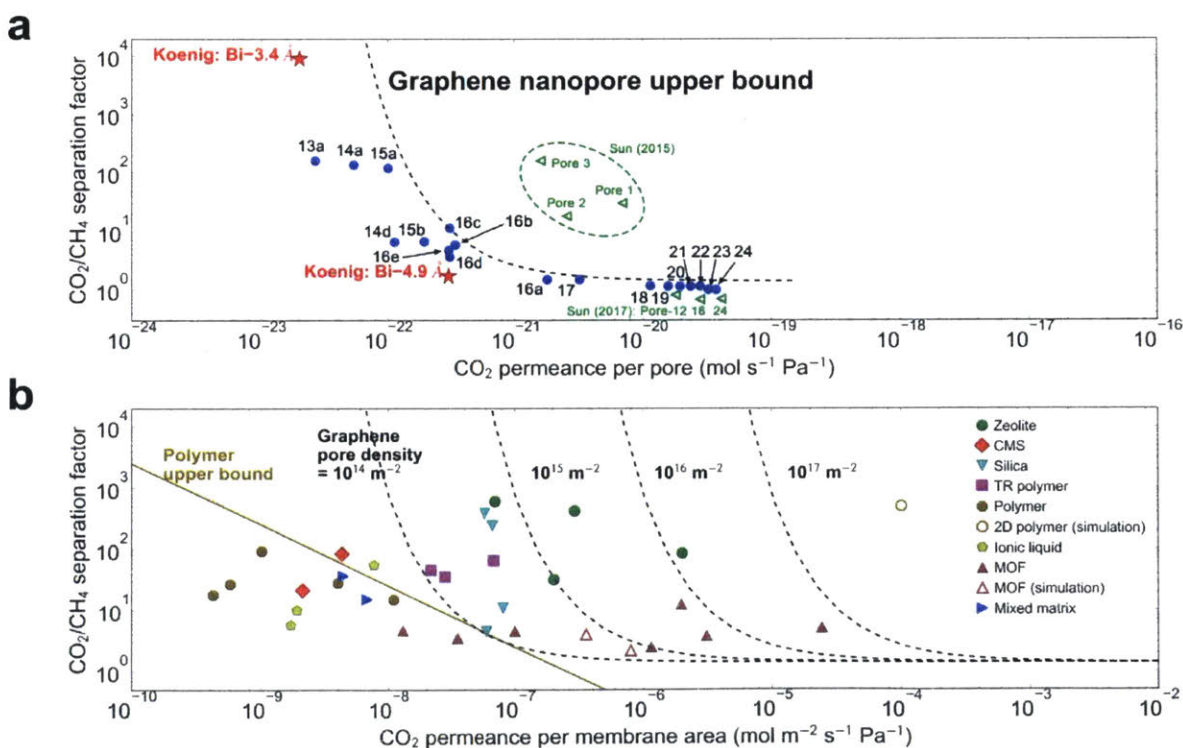
$$J = \frac{\text{Permeability}}{\text{thickness}} \Delta p \quad (1.1)$$

The inverse dependence on thickness often means thin structures are favored in conventional polymeric membranes, though the lower bounds of thickness are limited by structural consideration and a more pronounced drop in separation factors due to defects. A single layer graphene membrane can withstand large pressures over micron sized holes, demonstrated with 3MPa differential over 5 $\mu\text{m}$  diameter circular orifice.<sup>20</sup> With a suitable support structure, graphene acts as the ultimate limit in the pursuit of thin membranes at just one atom thick.

The limits of conventional membranes are often represented by a so called “Robeson plot,” which plots the empirical tradeoff observed between separation selectivity and permeability of the membrane; membranes with higher selectivity tend to have lower overall throughput for an equivalent thickness.<sup>31</sup> Permeability, flux



normalized by driving pressure and membrane thickness, is not an appropriate measure for vanishingly thin graphene, but for the sake of comparison, a similar plot can be created using selectivity (separation factor) and permeance, which is flux normalized by driving pressure, as shown in Figure 3. Yuan and coworkers predicted the results for the separation given the range of different pore sizes, and plotted the empirical fit to those results, demonstrating the tradeoff between larger permeance with larger pores and higher selectivity with smaller pores, alongside results for other membranes in the literature. The results show that graphene membranes can exceed the Robeson limits for polymeric membranes, and at high pore density, also match or exceed the performance of other newer membrane architectures such as Zeolites and MOFs.



**Figure 3:** (a) Robeson plot (separation factor vs permeance per pore) characterizing the CO<sub>2</sub>/CH<sub>4</sub> separation through various graphene sub-nanometer pores at 300 K. Pore configuration identifiers are annotated beside each data point. Experimental data obtained by Koenig et al.<sup>32</sup> and

results from several MD simulations<sup>33, 34</sup> are also plotted. (b) Comparison between a porous graphene membrane and other membranes for CO<sub>2</sub>/CH<sub>4</sub> separations. Hollow markers correspond to simulation results. For the MOF membrane simulation work,<sup>35</sup> the MOF membranes are only ~5 nm thick in simulation. From a practical perspective, we calculated the permeance assuming a typical MOF membrane thickness of 5  $\mu\text{m}$ .<sup>36</sup> Reprinted with permission from Yuan, Z. *et al. ACS Nano* 11, 7974-87 (2017). Copyright 2017 American Chemical Society.<sup>37</sup>

DNA has been observed to pass through graphene pores, which is a first step towards potential application to DNA sequencing.<sup>38-40</sup> Some have used theory to explore tunneling effects with graphene membranes to achieve isotopic separations.<sup>11, 41-44</sup> Theoretical work has also shown that graphene membranes could act as membranes for desalination.<sup>24</sup>

There have now been multiple experimental demonstrations of membrane systems from single or few layer graphene. A study by the Bunch group showed that pores created by UV ozone etching in mechanically exfoliated graphene suspended over microcavities in silicon and demonstrating molecular sieving, creating high selectivities between gas species of differing molecular size.<sup>32, 45</sup> Work using the intrinsic defects in CVD grown graphene transferred onto polycarbonate track etched membranes in aqueous systems was able to demonstrate modest separation of larger molecules and investigated layer stacking to reduce the leakage through those intrinsic defects.<sup>46, 47</sup> Other work with the aqueous phase used a contact seal between a micron scale pipet tip and graphene at the air-water interface to measure conductivity through CVD graphene.<sup>48</sup> Another study used focused ion beam to create pore size distributions centered on multiple sizes from 8 nm to 1  $\mu\text{m}$  in two stacked layers of CVD grown graphene, transferred to and supported on a SiN<sub>x</sub>

membrane, and demonstrated Knudsen selectivity based on the square root of molecular weight typical of classical effusion.<sup>49</sup> Recent work with larger scale membranes has also began to show some selectivity from molecular sieving effects,<sup>50</sup> previously only seen in small scale membranes. Other work has demonstrated proton transport through pristine, mechanically exfoliated graphene, as well as other 2D crystals, coated with Nafion and suspended across a hole drilled through SiN<sub>x</sub>.<sup>8</sup>

Graphene represents a fundamentally new type of membrane active layer, since it is only a single carbon atom thick. While a typical membrane possesses a mass transport resistance that scales inversely with thickness, single layer graphene represents the extreme limit of negligible thickness. Hence, continuum equations that are frequently employed for membrane analysis do not apply to the case of SLG. Moreover, the external surface of the membrane that is orthogonal to the transport direction is almost always neglected in the analysis of conventional membranes. In an MD study of H<sub>2</sub>/N<sub>2</sub> separation via a graphene membrane, it was shown that, for certain pore sizes, the nitrogen permeation rate could exceed that of hydrogen due to increased adsorption of the larger molecules.<sup>1</sup> This is contrary to the expectation that the smaller molecules should have a higher permeation rate. However, as will be shown, the external surface is expected to dominate molecular transport in many cases involving SLG membranes. Other molecular dynamics simulations have also shown an importance of the adsorbed phase.<sup>9, 12</sup> We derive analytical expressions for several relevant mechanisms of gas permeation through SLG membranes involving both strongly and weakly adsorbing gases. These mechanisms are then used to predict the results of a separation of hydrogen and nitrogen for pores of various sizes. We show that for larger pores, the more strongly

adsorbing nitrogen permeates faster than weakly adsorbing hydrogen. We also show and explain that the permeation rate is expected relatively constant across various larger nanopores in SLG membranes.

The Bunch group's demonstration of molecular sieving<sup>32</sup> and investigation of mechanical properties<sup>20</sup> uses mechanically exfoliated graphene suspended over a microcavities in a silicon wafer to form a membrane between the gas trapped in the microcavity and the atmosphere; measuring the deflection of the graphene surface over time is used to track the transport of gas. While this technique is not scalable, it does offer the unique advantage of being able to measure the transport characteristics of a single or few subnanometer pores, giving a window towards the fundamental transport characteristics of graphene. This platform has demonstrated switchable gating of the transport by gold nanoclusters on the graphene membrane surface, as well as smaller but significant fluctuations in transport without gold nanoclusters present.<sup>45</sup> We present the first mathematical analysis of stochastic gas permeation through any membrane/nanopore system. We validate the model using experimental results from our previous work on single layer graphene membranes under batch depletion conditions parametric in starting pressure for He, H<sub>2</sub>, Ne, and CO<sub>2</sub> between 100 and 670 kPa.<sup>45</sup> The model enables one to use membrane deflection curves parametric in starting pressure to confirm a time dependent membrane permeance (pressure normalized molecular flow). Stochastic fluctuations of the gas permeance can be analyzed using a Hidden Markov model to fit discrete states and estimate the activation barrier for switching. Our formalism also teaches how to use the relations between the states given by the Markov network for a collection of pores to determine the operative number that describe the data.

## 1.2 Application of Nanoscale Transport to a Nanonozzle

Further, we apply our familiarity with nanopores to the exploration of using a nanopore as a “nanonozzle” to deliver a gaseous reagent locally and grow nanoscale features via a CVD type reaction. The concept could apply generally,

We focus on the specific example of the synthesis of graphene nanoribbons, which are of interest for graphene’s high conductance and its bandgap that forms due to confinement in a nanoribbon. Ebeam lithography is often used for nanopatterning,<sup>51</sup> including nanoribbons,<sup>52</sup> though graphene nanoribbons from lithographic techniques typically lose conductance due to lack of control over the resulting edge structure. Other methods for creating graphene nanoribbons include templated growth using a surface structure<sup>53</sup>, and the unzipping of carbon nanotubes on a surface into nanoribbons,<sup>54</sup> though so far these methods have lacked the ability to shape or place the ribbon as desired. Dip pen nanolithography is another tool for nanopatterning, useful for depositing material compatible as an ink,<sup>55</sup> but is ill suited for controlled delivery of precursors for higher temperature CVD reactions that can give pristine lattices and edges. The idea of performing a local reaction on the nanoscale is similar to the approach of inducing a reaction with a laser<sup>56</sup>, as well as general lithography. The design is similar to previously developed “nanojets,” which used energetic plasma to etch away a surface to form a structure,<sup>57</sup> or used laser ablation to release and deliver larger molecules locally.<sup>58</sup> However, the key aspect of the nanonozzle concept explored here is that the structure and nanoscale is derived from the moving local delivery and diffusion of the reagent to create a concentration gradient that. We will use analytical models and simple simulations to

explore the relevant parameters and considerations for the design of a nanonozzle system capable of growing a nanoribbon with a CVD reaction.

## 2 THEORY OF 2D MEMBRANE TRANSPORT

### 2.1 Significance of 2D Membrane Theory

Graphene has enormous potential as a unique molecular barrier material with atomic layer thickness, enabling new types of membranes for separation and manipulation. However, the conventional analysis of diffusive transport through a membrane fails in the case of single layer graphene (SLG) and other 2D atomically thin membranes. In this chapter, analytical expressions are derived for gas permeation through such atomically thin membranes in various limits of gas diffusion, surface adsorption, or pore translocation as the rate limiting step. Gas permeation can proceed via direct gas phase interaction with the pore, or interaction via the adsorbed phase on the membrane exterior surface. A series of van der Waals force fields allow for the estimation of the energy barriers present for various types of graphene nanopores. These analytical models will assist in the understanding of molecular dynamics and experimental studies of such membranes.

Graphene represents a fundamentally new type of membrane active layer, since it is only a single carbon atom thick. While a typical membrane possesses a mass transport resistance that scales inversely with thickness, single layer graphene represents the extreme limit of negligible thickness. Hence, continuum equations that are frequently employed for membrane analysis do not apply to the case of SLG. Moreover, the external surface of the membrane that is orthogonal to the transport direction is almost always neglected in the analysis of conventional membranes. In a recent MD study of  $H_2/N_2$  separation via a graphene membrane, it was shown that, for certain pore sizes, the

nitrogen permeation rate could exceed that of hydrogen due to increased adsorption of the larger molecules.<sup>1</sup> This is contrary to the expectation that the smaller molecules should have a higher permeation rate. However, as we show in this chapter, the external surface is expected to dominate molecular transport in many cases involving SLG membranes. Other molecular dynamics simulations have also shown an importance of the adsorbed phase.<sup>9, 12</sup> In this chapter, we derive analytical expressions for several relevant mechanisms of gas permeation through SLG membranes involving both strongly and weakly adsorbing gases. These mechanisms are then used to predict the results of a separation of hydrogen and nitrogen for pores of various sizes. We show that for larger pores, the more strongly adsorbing nitrogen permeates faster than weakly adsorbing hydrogen. We also show and explain that the permeation rate is expected relatively constant across various larger nanopores in SLG membranes. Descriptions for all variables appearing in this chapter are given in Table 1.

**Table 1:** Description of all variables and constants used in the derivation of the model and limits.

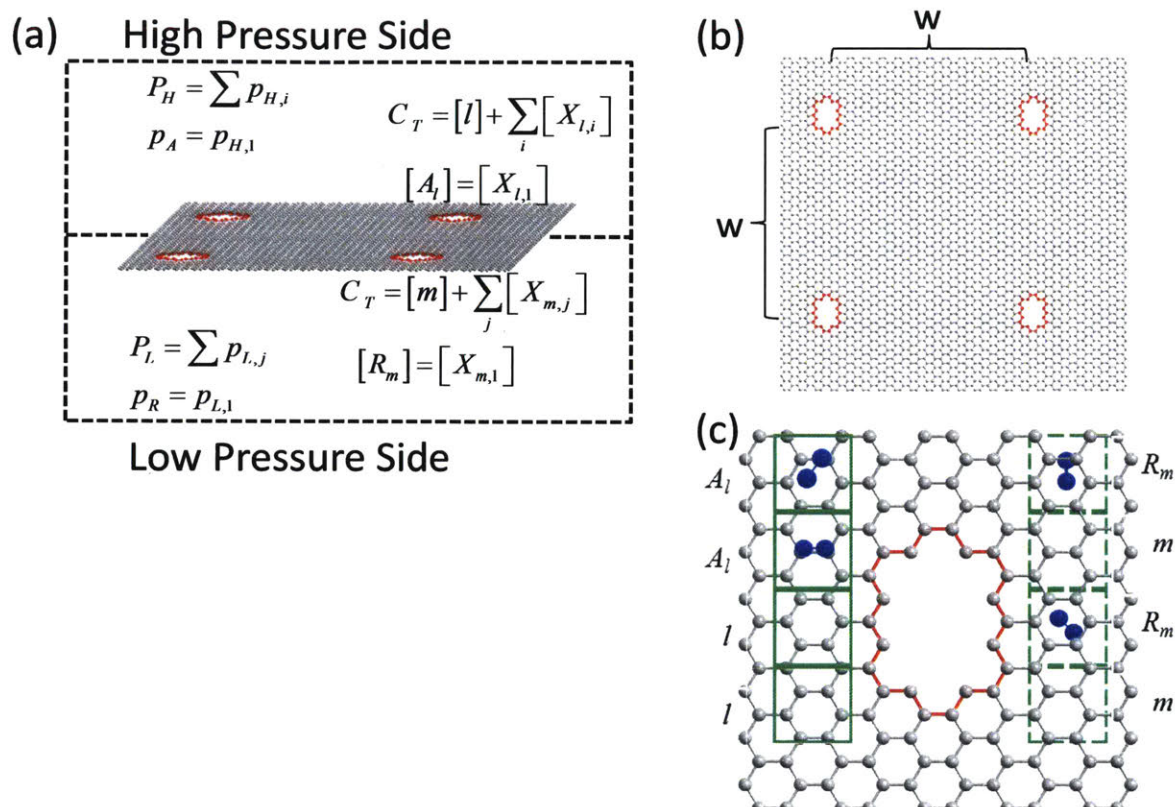
$P_H$	total pressure on high pressure side
$P_{H,i}$	partial pressure of <i>i</i> th species on high pressure side
$p_A$	partial pressure of species <i>i</i> =1 on high pressure side
$P_L$	total pressure on low pressure side
$p_{L,i}$	partial pressure of <i>i</i> th species on low pressure side
$p_R$	partial pressure of species <i>i</i> =1 on low pressure side
$C_T$	total surface sites per area
$[l]$	surface concentration of empty sites on high pressure side of SLG
$[X_{l,i}]$	surface concentration of <i>i</i> th species on high pressure side of SLG
$[A_l]$	surface concentration of species <i>i</i> =1 on high pressure side of SLG
$[m]$	surface concentration of empty sites on low pressure side of SLG
$[X_{m,i}]$	surface concentration of <i>i</i> th species on low pressure side of SLG



$[R_m]$	surface concentration of species $i=1$ on low pressure side of SLG
$w$	pitch of pores in SLG for square tiling
$\dot{n}$	impingement rate at a surface from gas phase
$A$	active area for impingement from gas phase
$\Delta P$	pressure drop from high pressure side to low pressure side
$M$	molecular weight
$R$	ideal gas constant
$T$	temperature
$J_{i,gas}$	flux through a graphene membrane via gas phase impingement
$C_B$	surface density of pores
$s_B$	effective surface area per pore
$E_{a,gas,i}$	activation energy for $i$ th species to pass through the pore from the gas phase
$[B_l]$	surface concentration of pores that are empty on the high pressure side
$[AB_l]$	surface concentration of pores with species $i=1$ associated on the high pressure side
$[R_m]$	surface concentration of pores that are empty on the low pressure side
$[RB_m]$	surface concentration of pores with species $i=1$ associated on the low pressure side
$k_j$	forward rate constant of the $j$ th step, for species $i=1$
$k_{-j}$	reverse rate constant of the $j$ th step, for species $i=1$
$K_j$	equilibrium constant of the $j$ th step, for species $i=1$
$s_A$	surface area per adsorbed species $i=1$
$\theta_A$	fraction of monolayer coverage on high pressure side of SLG defined by Langmuir adsorption model, for species $i=1$
$\theta_R$	fraction of monolayer coverage on low pressure side of SLG defined by Langmuir adsorption model, for species $i=1$
$J_j$	flux via adsorbed phase assuming $j$ th step is rate limiting, for species $i=1$
$\theta_{H/L,i}$	fraction of monolayer coverage on high/low pressure side of SLG defined by Langmuir adsorption model, for $i$ th species
$K_{j,i}$	equilibrium constant of $j$ th step, for $i$ th species
$E_{a,j}$	activation energy for $j$ th step

## 2.2 Results and Discussion

There are several analogies between molecular permeation through an SLG membrane and catalytic chemical reaction of a molecule at an active site on the surface. Both can proceed by a preliminary adsorption step to the surface, followed by surface diffusion to the active site (or open pore) or by direct interaction of the molecule with the active site from the gas phase (the Eley-Rideal mechanism in catalysis). Adsorption into and transport across the graphene nanopore can be controlled by an activation energy if the constriction is small enough, analogous to the activation energy for chemical reaction at a catalytic active site. Because of this analogy, it will be useful to label the permeating species on the high pressure side the membrane as  $A$ , and the species on the low pressure side  $R$ , with a transition from  $A \rightarrow R$  corresponding to spatial transport through the SLG membrane along the chemical potential gradient through the pore. Similarly, the pore will be considered a species and labeled as  $B$ .



**Figure 4:** Schematic for a SLG gas separation membrane that divides reservoirs of gas at high pressure ( $P_H$ ) containing species at partial pressure  $p_{H,i}$  for species  $i$  and low pressure  $P_L$  containing partial pressure  $p_{L,i}$ . The gas component is labeled  $A_i$  on the high pressure side and  $R_i$  after permeation through to the low pressure side. The membrane contains  $CT$  total number of sites of gas adsorption on the SLG surface per area, with unoccupied sites  $l$  and those occupied  $X_{l,i}$  for species  $i$  for the high pressure side. The low pressure side has unoccupied sites  $m$  and occupied sites  $X_{m,i}$  for species  $i$ . Pores of radius  $r_p$  have a pitch of  $w$  in a square tiling. Reprinted with permission from Drahusluk, L.W. et al. *Langmuir* 28, 16671-78 (2012). Copyright 2012 American Chemical Society.<sup>14</sup>

Consider a single layer graphene (SLG) membrane separating two gas reservoirs held at pressures  $P_H$  and  $P_L$ , with  $\Delta P = P_H - P_L$ ; the partial pressure of species 1 in the two reservoirs will be called  $p_A$  and  $p_R$  respectively. The SLG contains  $C_B$  pores/area of

radius  $r_B$  equally spaced at a pitch of  $w$  nm in a 2D rectangular lattice, and the surface density of available adsorption sites, or the surface density of a monolayer of adsorbed gas, is  $C_T$ .  $C_T$  is assumed to be equivalent for all gas species. As the high pressure and low pressure surfaces are two faces of the same SLG, the density of pores,  $C_B$ , and the density of possible adsorption sites,  $C_T$ , is identical for both sides. On the high pressure side of the SLG, a surface site that is occupied by an adsorbed gas molecule of the  $i^{\text{th}}$  species is labeled as  $X_{m,i}$ , and an empty area of the same size is considered an unoccupied site and labeled as  $l$ . In order to distinguish between the two faces of the SLG, on the low pressure side, occupied and unoccupied sites are labeled as  $X_{m,i}$  and  $m$  respectively. We neglect the influence of the hypothetical support underneath the SLG membrane as having much lower mass transport resistance than the SLG membrane. We assume that the pore is symmetrical with respect to the plane of the graphene. In Figure 4, the pore depicted is model pore type  $a$  from Figure 6.

### 2.2.1 Gas phase pathway

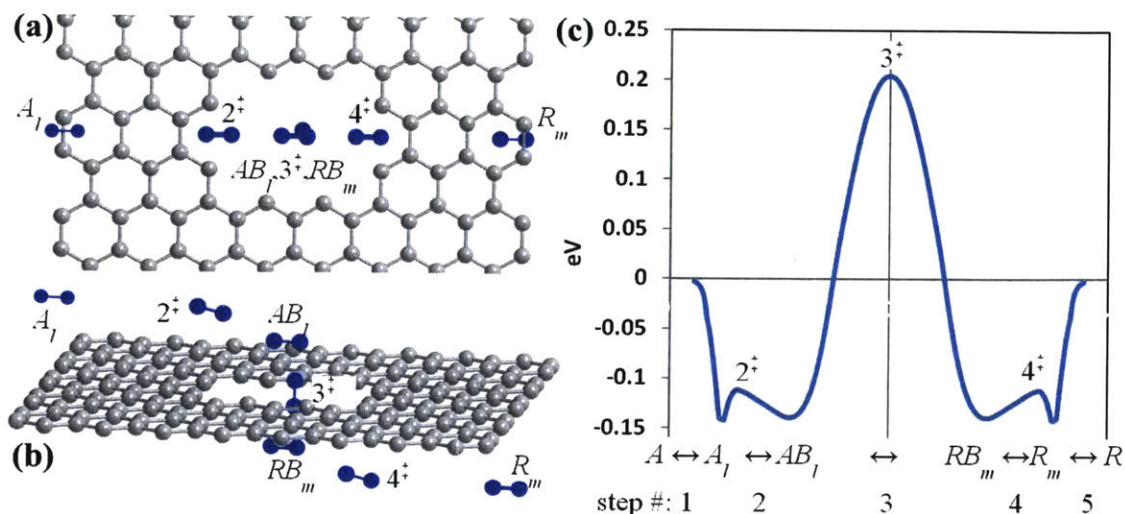
For steric selectivity in gas separation, pores in graphene membranes should have dimensions near and below 1 nm. This is small enough that transport occurs in the molecular regime and Poiseuille flow is negligible. The solution for gas transport through a vanishingly thin orifice was described by Knudsen,<sup>59</sup> and is simply the impingement rate,  $\dot{n}$ , upon the area of the pore given by equation (2.1). The inclusion of Arrhenius dependence in equation (2.2) gives the flux,  $J_{i,gas}$ , accounting for the energy barrier the molecule experiences passing through the pore.

$$\dot{n} = A \frac{\Delta P}{\sqrt{2\pi M RT}} \quad (2.1)$$

$$J_{i, gas} = C_B s_B \left( \frac{-1}{\sqrt{2\pi M RT}} \right) e^{-E_{a, gas, i}/RT} \Delta p_i \quad (2.2)$$

$s_B$  is the effective surface area per pore,  $M$  is the molecular weight, and  $E_{a, gas, i}$  is the energy barrier height relative to the gas phase. For larger pores, the effective surface area per pore,  $s_B$ , is approximately the simple geometric area of the open lattice space. For smaller pores, where the translocating molecule is commensurate with the size of the pore, along with an energy barrier,  $E_{a, gas}$ , becoming relevant, the effective surface area per pore,  $s_B$ , will be smaller than the geometric outline of vacancy, as only impingement on or near the center of the pore will result in transport through the graphene, analogous to empirical corrections to transport models for small pore sizes aluminas or similar.<sup>60, 61</sup>

### 2.2.2 Adsorbed phase pathway



**Figure 5:** Nitrogen passing through a decavacancy pore. (a) Top view (b) Side view (c) Calculated vdW energy coordinate. Interaction energy calculated with Lennard-Jones potential.<sup>1</sup> Reprinted with permission from *Drahushuk, L.W. et al. Langmuir 28, 16671-78 (2012)*. Copyright 2012 American Chemical Society.<sup>14</sup>

**Table 2:** Five elementary steps of adsorbed phase pathway and corresponding rate of each step.

step #	step	rate
1	$l + A \xrightleftharpoons{k_1} A_l$	$k_1 p_A [l] - k_{-1} [A_l]$
2	$A_l + B_l \xrightleftharpoons{k_2} AB_l + l$	$k_2 [A_l][B_l] - k_{-2} [AB_l][l]$
3	$AB_l \xrightleftharpoons{k_3} RB_m$	$k_3 [RB_m] - k_{-3} [AB_l]$
4	$RB_m + m \xrightleftharpoons{k_4=k_{-2}} R_m + B_m$	$k_4 [RB_m][m] - k_{-4} [R_m][B_m]$
5	$R_m \xrightleftharpoons{k_5=k_{-1}} m + R$	$k_5 [R_m] - k_{-5} p_R [m]$

In the adsorbed phase pathway, shown by Figure 5, the species passes through four states on the surface of the graphene and five individual steps. First, a gas phase

molecule adsorbed to a site (step 1) on the surface. Second, the molecule diffuses to a pore (step 2) and associates into a potential well positioned in the space above the pore. Third, the molecule associated over the pore passes through the pore (step 3) to be associated with the pore on the downstream side of the graphene. Fourth, the molecule disassociates from the area above the pore (step 4) onto the downstream surface of the graphene. Fifth and finally, the molecule desorbs from the surface (step 5) and enters the gas phase on the downstream side of the graphene. For simplicity we will derive analytical solutions for the limits of this model assuming only a single adsorbing component. The corresponding results for multiple adsorbing species are given at the end. A previous analytical model for the adsorbed phase specialized in the limit of maximum porosity.<sup>11</sup> Table 2 summarizes the steps in reaction kinetics notation; the rate constants for the forward and reverse for the  $i$ th step are given by  $k_i$  and  $k_{-i}$  respectively.

The definitions for equilibration of each of the five mechanistic steps are given in equations (2.3) to (2.7). The definition of the 3<sup>rd</sup> equilibrium constant as unity is a result of the assumption that the pore is symmetric about the plane of the graphene.

$$K_1 = \frac{k_1}{k_{-1}} = \frac{[A_l]}{p_A [l]} \quad (2.3)$$

$$K_2 = \frac{k_2}{k_{-2}} = \frac{[AB_l][l]}{[A_l][B_l]} \quad (2.4)$$

$$K_3 = \frac{k_3}{k_{-3}} = \frac{[AB_l]}{[RB_m]} = 1 \quad (2.5)$$

$$K_4 = \frac{k_4}{k_{-4}} = \frac{[R_m][B_m]}{[RB_m][m]} = 1/K_2 \quad (2.6)$$

$$K_5 = \frac{k_5}{k_{-5}} = \frac{p_R[m]}{[R_m]} = 1/K_1 \quad (2.7)$$

A site balance on the surface area of the graphene, accounting for area occupied by pores, yields equation (2.8), where  $s_A$  is the surface area per adsorbed species. Similarly, a balance on the number of free and occupied pores yields equation (2.9).

$$C_T = \frac{1}{s_A} - \frac{C_B s_B}{s_A} = [l] + [A_l] = [m] + [R_m] \quad (2.8)$$

$$C_B = [B_l] + [AB_l] = [B_m] + [RB_m] \quad (2.9)$$

By applying the surface site balance equation (2.8) along with the equilibrium definition for the adsorption equation (2.3), the equilibrium surface concentrations can be derived in as in equations (2.11) and (2.12). This is the result using the Langmuir model of adsorption, which assumes adsorption is limited to a single monolayer, the energy of adsorption is independent of coverage, and that all adsorption sites are equivalent. It is often convenient to use the variable  $\theta_A$ , the fraction of monolayer coverage, given by equation (2.10).

$$\theta_A = \frac{K_1 p_A}{1 + K_1 p_A} \quad (2.10)$$

$$[A_l] = C_T \theta_A = C_T \frac{K_1 p_A}{1 + K_1 p_A} \quad (2.11)$$



$$[I] = C_T(1 - \theta_A) = C_T \frac{1}{1 + K_1 p_A} \quad (2.12)$$

If equilibrium is achieved for surface species associating to the pore, then equations (2.9), (2.11), and (2.12) can be used to derive the number of occupied and unoccupied pore sites. These results are given by equations (2.13) and (2.14).

$$[B_l] = \frac{C_B(1 - \theta_A)}{(1 + (K_2 - 1)\theta_A)} \quad (2.13)$$

$$[AB_l] = \frac{C_B K_2 \theta_A}{(1 + (K_2 - 1)\theta_A)} \quad (2.14)$$

With these results, it is possible to describe the surface concentrations in terms of equilibrium concentrations and the bulk pressure. Equations (2.11), (2.12), (2.13), and (2.14) describe the surface in equilibrium with the upstream surface of graphene. As the graphene surfaces (H and L) are symmetric, equivalent expressions can be written for surface concentrations in equilibrium with the downstream bulk. In order to derive tractable expressions for the rates of permeation, we will derive limits assuming various rate limiting steps, with all other steps in equilibrium.

Assuming step 1, adsorption to the graphene surface, is rate limiting.

$$\begin{aligned} J_1 &= k_1 p_A [I] - k_{-1} [A_l] \\ J_1 &= k_1 p_A ([m]) - k_{-1} ([R_m]) \end{aligned} \quad (2.15)$$

The resulting expression for adsorption to the graphene surface rate limiting is equation (2.16).

$$J_1 = k_1 p_A \left( \frac{C_T}{1 + K_1 p_R} \right) - k_{-1} \left( \frac{C_T K_1 p_R}{1 + K_1 p_R} \right) \quad (2.16)$$

Assuming step 2, association to a pore site, is rate limiting.

$$\begin{aligned} J_2 &= k_2 [A_l][B_l] - k_{-2} [I][AB_l] \\ J_2 &= k_2 [A_l]((C_B - [RB_m])) - k_{-2} [I]([RB_m]) \end{aligned} \quad (2.17)$$

The resulting expression for association to a pore site rate limiting is equation (2.18).

$$J_2 = k_2 C_T \theta_A \frac{C_B (1 - \theta_R)}{(1 + (K_2 - 1) \theta_R)} - k_{-2} C_T (1 - \theta_A) \frac{C_B K_2 \theta_R}{(1 + (K_2 - 1) \theta_R)} \quad (2.18)$$

Assuming step 3, passage through a pore, is rate limiting.

$$J_3 = k_3 [AB_l] - k_{-3} [RB_m] \quad (2.19)$$

An assumption has been that the association of species to the two faces of the pore has been assumed independent. We have thus far not distinguished pores that have a molecule trapped on both sides of the pore entrance. If there are molecules on both sides of the pore, they may inhibit passage. The subsequent equations will show that accounting for this blocking results in the same overall rate.

First modify equation (2.19) to subtract any pores that have molecules on both faces of the pore from the rate expression. Then employing the fact that the forward and

reverse rate constants are identical for this step, equation (2.20) shows that the overall rate is the same.

$$\begin{aligned}
 J_3 &= k_3 ([AB_l] - [ABR]) - k_{-3} ([RB_m] - [ABR]) \\
 J_3 &= k_3 [AB_l] - k_{-3} [RB_m] + \underbrace{(k_3 - k_{-3})}_{=0} [ABR] \\
 J_3 &= k_3 [AB_l] - k_{-3} [RB_m]
 \end{aligned} \tag{2.20}$$

The resulting expression passage through the rate limiting is equation (2.21).

$$J_3 = k_3 \frac{C_B K_2 \theta_A}{(1 + (K_2 - 1) \theta_A)} - k_{-3} \frac{C_B K_2 \theta_R}{(1 + (K_2 - 1) \theta_R)} \tag{2.21}$$

Assuming step 4, disassociation from the pore site, is rate limiting.

$$\begin{aligned}
 J_4 &= k_4 [m] [RB_m] - k_{-4} [R_m] [B_m] \\
 J_4 &= k_4 [m] ([AB_l]) - k_{-4} [R_m] ([B_l])
 \end{aligned} \tag{2.22}$$

The resulting expression for disassociation from the pore site rate limiting is equation (2.23).

$$J_4 = k_4 C_T (1 - \theta_R) \frac{C_B K_2 \theta_A}{(1 + (K_2 - 1) \theta_A)} - k_{-4} \theta_R \frac{C_B (1 - \theta_A)}{(1 + (K_2 - 1) \theta_A)} \tag{2.23}$$

Assuming step 5, desorption from the graphene surface, is rate limiting.

$$\begin{aligned}
 J_5 &= k_5 [R_m] - k_{-5} p_R [m] \\
 J_5 &= k_{-A} ([A_l]) - k_{-5} p_R ([I])
 \end{aligned} \tag{2.24}$$

The resulting expression for adsorption to the graphene surface rate limiting is equation (2.16).

$$J_5 = k_5 \left( \frac{C_T K_1 p_A}{1 + K_1 p_A} \right) - k_{-5} p_R \left( \frac{C_T}{1 + K_1 p_A} \right) \quad (2.25)$$

The above derivation assumes that there is only a single species. It is possible to extend these results to multiple species, **assuming that all species have the same rate limiting step**. The resulting expressions are given by equations (2.27) to (2.31).

$$\theta_{H/L,i} = \left( \frac{K_{1,i} p_{H/L,i}}{1 + \sum K_{1,j} p_{H/L,j}} \right) \quad (2.26)$$

$$J_1 = k_1 p_A \left( \frac{C_T}{1 + \sum K_{1,j} p_{L,j}} \right) - k_{-1} \left( \frac{C_T K_{1,A} p_R}{1 + \sum K_{1,j} p_{L,j}} \right) \quad (2.27)$$

$$J_2 = k_2 C_T \frac{C_B \theta_A (1 - \sum \theta_{H,i})}{(1 + \sum (K_{2,i} - 1) \theta_{H,i})} - k_{-2} C_T \frac{C_B K_{2,A} \theta_R (1 - \sum \theta_{H,i})}{(1 + \sum (K_{2,j} - 1) \theta_{L,j})} \quad (2.28)$$

$$J_3 = k_3 \frac{C_B K_{2,A} \theta_A}{(1 + \sum (K_{2,i} - 1) \theta_{H,i})} - k_{-3} \frac{C_B K_{2,A} \theta_R}{(1 + \sum (K_{2,j} - 1) \theta_{L,j})} \quad (2.29)$$

$$J_4 = k_4 C_T \frac{C_B K_{2,A} \theta_A (1 - \sum \theta_{L,j})}{(1 + \sum (K_{2,i} - 1) \theta_{H,i})} - k_{-4} \theta_R \frac{C_B (1 - \sum \theta_{L,j})}{(1 + \sum (K_{2,j} - 1) \theta_{L,j})} \quad (2.30)$$

$$J_5 = k_5 \left( \frac{C_T K_{1,i} p_A}{1 + \sum K_{1,i} p_{H,i}} \right) - k_{-5} p_R \left( \frac{C_T}{1 + \sum K_{1,j} p_{H,j}} \right) \quad (2.31)$$

### 2.2.3 Diffusion limited case

In step 2, the molecule must both diffuse to the pore and overcome an activation barrier to position itself above the pore. The rate constant for this step is affected both by the diffusion properties and the activation energy. And may exhibit different behavior depending on which process dominates. If diffusion is the limiting process, then the concentration gradient can be described by the differential equation (2.32) as a function of radius,  $r$ , in cylindrical coordinates, which includes surface diffusion and adsorption/desorption. The boundary conditions are given by equations (2.33) and (2.34).  $D_i$  is the self-diffusion coefficient,  $r_{AB}$  is the sum of the radius of the pore and the adsorbed species.

$$0 = \frac{D_i}{r} \frac{d}{dr} \left( r \frac{dC_{Al}}{dr} \right) + (k_A p_A C_l - k_{-A} C_{Al}) \quad (2.32)$$

$$C_{Al}(r \rightarrow \infty) = C_{Al,eq} \quad (2.33)$$

$$k_s C_{Al}(r_{AB}) = 2\pi r_{AB} D_i \left. \frac{dC_{Al}}{dr} \right|_{r_{AB}} \quad (2.34)$$

With the inclusion of adsorption and desorption, the length scale,  $r_D$ , for the competition of diffusion with ad/desorption is given by equation (2.35).

$$r_D = \sqrt{\frac{D_i}{k_{-A}(1 + K_A p_A)}} \quad (2.35)$$

If the spacing between pores is larger than the length scale for diffusion, then the differential equation can be solved with an analytical solution. The apparent rate constant is defined with equation (2.36). The solution to (2.32), written in terms of modified Bessel functions of the second kind, is given by equation (2.37).<sup>62</sup>

$$k_{app} = k_s \frac{C_{Al}|_{r_{AB}}}{C_{Al,eq}} \quad (2.36)$$

$$k_{app} = \frac{k_s \left[ 2\pi D_i \left( \frac{r_{AB}}{r_D} \right) \frac{K_1 \left( \frac{r_{AB}}{r_D} \right)}{K_0 \left( \frac{r_{AB}}{r_D} \right)} \right]}{k_s + \left[ 2\pi D_i \left( \frac{r_{AB}}{r_D} \right) \frac{K_1 \left( \frac{r_{AB}}{r_D} \right)}{K_0 \left( \frac{r_{AB}}{r_D} \right)} \right]} \quad (2.37)$$

As  $r_D \ll r_{AB}$ , equation (2.37) simplifies to equation (2.38).

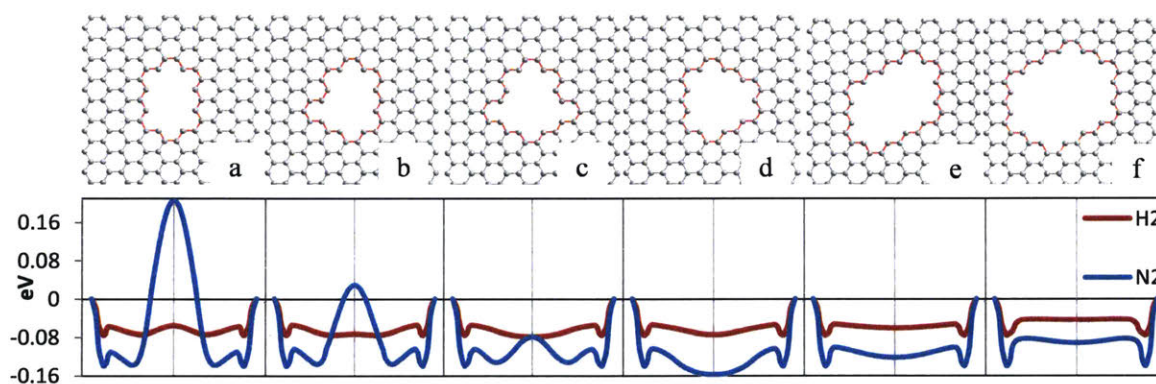
$$k_{app} \approx \frac{k_s \left( 2\pi \sqrt{k_{-A}(1+K_A p_A)} D_i r_{AB} \right)}{k_s + \left( 2\pi \sqrt{k_{-A}(1+K_A p_A)} D_i r_{AB} \right)} \quad (2.38)$$

This compares to the more commonly used result for diffusion-limited reactions in solutions given by equation (2.39).

$$k_{app, solution} = \frac{k_s (4\pi D r_{ab})}{k_s + (4\pi D r_{ab})} \quad (2.39)$$

### 2.2.4 Model Pores

We will examine six model pores, along with their van der Waals energy coordinates for nitrogen and hydrogen molecules. The pores and energy coordinates are depicted in Figure 6; the values for activation energies for the various steps depicted in Figure 6 are summarized in Table 3. Energies are obtained using multicenter Lennard-Jones calculations.<sup>1</sup> Without edge termination, these model pores are unlikely to be stable in a real graphene sheet. However, we will use these simple pores to represent real pores of over a range sizes.



**Figure 6:** Six model pores formed by removing (a) 10, (b) 11, (c) 12, (d) 13, (e) 22, and (f) 32 carbon atoms from a graphene lattice, along with energy coordinate for permeation through the pore (see **Figure 5**) for both hydrogen and nitrogen. Reprinted with permission from *Drahushuk, L.W. et al. Langmuir* 28, 16671-78 (2012). Copyright 2012 American Chemical Society.<sup>14</sup>

**Table 3:** Summary of activation energies for the six pores shown in Figure 6. Energies are calculated via Lennard Jones potential.<sup>1</sup>

pore	H <sub>2</sub> (eV)					N <sub>2</sub> (eV)				
	E <sub>a,2</sub>	E <sub>a,3</sub>	E <sub>a,4</sub>	E <sub>a,5</sub>	E <sub>a,gas</sub>	E <sub>a,2</sub>	E <sub>a,3</sub>	E <sub>a,4</sub>	E <sub>a,5</sub>	E <sub>a,gas</sub>
a	0.017	0.019	0.017	0.076	-	0.029	0.344	0.028	0.141	0.205
b	0.021	0.002	0.021	0.076	-	0.036	0.165	0.032	0.141	0.028
c	0.020	-	0.024	0.076	-	0.035	0.053	0.028	0.141	-
d	0.021	-	0.021	0.076	-	0.036	-	0.054	0.141	-
e	0.022	-	0.008	0.076	-	0.039	-	0.021	0.141	-
f	0.033	-	0.001	0.076	-	0.057	-	0.009	0.141	-

### 2.2.5 Model Parameters

We have presented a model for the permeation through graphene membranes via an adsorbed phase, and presented equations describing the permeation rate for various limits of our model. To make use of the equations, estimates for the various parameters are necessary. Without intensive effort, it is possible to make estimates that should be within a few orders of magnitude and can provide insight on which of the steps is most likely to be limiting.

Adsorption studies have not been focused on a single monolayer of graphene, however there are ample studies of adsorption to carbon nanotubes and graphite, which would be expected to be reasonable analogs for monolayer graphene. The adsorption equilibrium properties of some gases on monolayer graphene have also been calculated.<sup>63</sup> A simple kinetic model for the desorption is given by equation (2.40).<sup>64</sup> One interpretation of this estimation is the vibration frequency normal to the surface, therefore this rough estimation can also be applied for the rate at which a species associated directly above the pore will pass over the energy barrier through the pore. An order of magnitude estimate for the terms in the pre-exponential factor is  $10^{13}$  1/s.<sup>64</sup>



$$k = \kappa \frac{k_B T}{h} \frac{q^\ddagger}{q_a} \exp\left(-\frac{E_a}{RT}\right) \quad (2.40)$$

For the forward rate constant of the second step, the 2D ideal gas collision theory can provide an estimation, given by equation (2.41), where  $P_s$  is a steric factor between 0 and 1,  $\sigma_{AB}$  is the sum of the two radiuses, and  $\mu_{AB}$  is the moment which simplifies to the mass of the gas molecule in this case. For nitrogen and a 1 nm pore, this results in a pre-exponential factor of  $\sim 10^{17}$  m<sup>2</sup>/s/mol. The equilibrium coefficient for the 3<sup>rd</sup> reaction is 1 as the membrane is symmetric.

$$k = 2P_s \sigma_{AB} \sqrt{\frac{\pi k_B T}{2\mu_{AB}}} \exp\left(-\frac{E_a}{RT}\right) \quad (2.41)$$

Using these models, we estimate nitrogen's parameters for two of the pores, (a) and (c), in Figure 6 that were used in a recent molecular dynamics simulation examining H<sub>2</sub> and N<sub>2</sub>.<sup>1</sup> As a simplifying assumption, we will set the value of equilibrium constant to 1 for the second and fourth steps, which are the association and dissociation of a molecule on the surface to the pore. We expect the true value of the step 2 equilibrium constant to be less than 1, as a molecule suffers an entropic loss by associating to the pore from the 2D ideal gas, in addition to a slight potential energy difference between those two states. A value of  $10^{-5}$  mol/m<sup>2</sup> is used for  $C_T$ , from the inverse of nitrogen's surface area per molecule. A value of  $8.8 \times 10^{-8}$  mol/m<sup>2</sup> is used for  $C_B$  to match the setup of literature molecular dynamic simulation.<sup>1</sup> For comparison, a recent ion beam exposure technique achieved a nanopore density of  $8 \times 10^{-9}$  mol/m<sup>2</sup> in SLG.<sup>65</sup> The results modeling single species N<sub>2</sub> permeation are given in Table 4.

**Table 4:** Comparison of the equations derived for each step rate limiting to the numerical result of the full model for pores (a) and (c) from **Figure 6**. Assuming single species, nitrogen,  $P_H=0.2$  MPa,  $P_L=0.0$  MPa, and  $K_I=3$  1/MPa.<sup>30</sup>

Limit	$E_a$ (eV)		$k_i$		N <sub>2</sub> permeation rate (mol/m <sup>2</sup> /s)	
	pore (a)	pore (c)	pore (a)	pore (c)	pore (a)	pore (c)
1: eq (2.27) adsorption to surface	-	-	$1 \times 10^6$ 1/Pa/s	$1 \times 10^6$ 1/Pa/s	$2.5 \times 10^5$	$2.5 \times 10^5$
2: eq (2.28) association to pore	0.029	0.035	$1 \times 10^7$ m <sup>2</sup> /mol/s	$7 \times 10^{16}$ m <sup>2</sup> /mol/s	$3.2 \times 10^4$	<b><math>2.5 \times 10^4</math></b>
3: eq (2.29) traversal of pore	0.344	0.053	$2 \times 10^7$ 1/s	$1 \times 10^{12}$ 1/s	<b><math>4.9 \times 10^{-1}</math></b>	<b><math>3.4 \times 10^4</math></b>
4: eq (2.30) dissociation from pore	0.028	0.028	$1 \times 10^7$ m <sup>2</sup> /mol/s	$1 \times 10^{17}$ m <sup>2</sup> /mol/s	$3.2 \times 10^4$	<b><math>2.8 \times 10^4</math></b>
5: eq (2.31) desorption from surface	0.141	0.141	$4 \times 10^{10}$ 1/s	$4 \times 10^{10}$ 1/s	$1.5 \times 10^5$	$1.8 \times 10^5$
numerical solution	-	-	-	-	<b><math>4.9 \times 10^{-1}</math></b>	<b><math>8.7 \times 10^3</math></b>

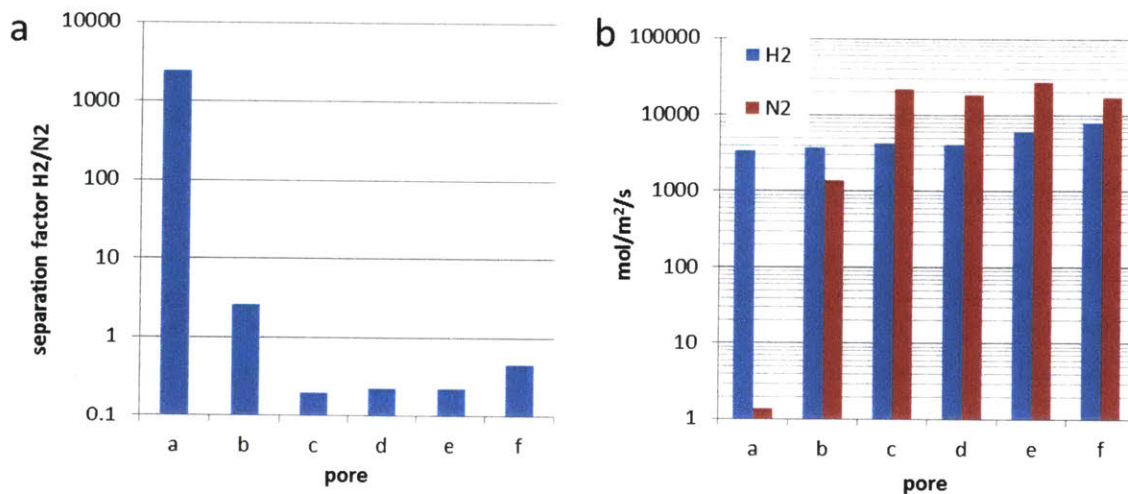
In addition to the analytical results made by assuming a rate limiting step, it is also possible to generate a steady state numerical solution by solving for the differential equations derived from the rate expression for the five individual steps (see Table 2). For pore (a) in Table 4, the limit corresponding the transversal of the pore (step 3) perfectly matches the numerical solution result, indicating that step three is rate limiting. For pore (c) in Table 4, no equation perfectly matches the numerical solution and multiple limits provide rates of a comparable order of magnitude. This indicates that no single step is rate limiting; and while none of the analytical solutions apply exactly, they do still provide an answer within an order of magnitude of the numerical result.

The conditions used here, while not exactly the same, were similar to a previous molecular dynamics study.<sup>1</sup> The nitrogen permeation seen in the original MD results<sup>1</sup> is several orders of magnitude smaller for both pores considered. In general, the simple models used here carry a higher level of uncertainty than a more detailed investigation. Ignoring steric factors for all reaction rate constants is one reason the rate constants here are likely to be overestimates.

Our analysis demonstrates that the most significant steps influencing transport are 2, 3, and 4 as these are most likely to be rate limiting. For H<sub>2</sub>/N<sub>2</sub> separation, the simulation in ref<sup>1</sup> demonstrates that, for large pores (16-32 atom vacancies), the nitrogen permeation rate is nearly constant, while hydrogen permeation increases linearly with pore area. This indicates that the permeation of nitrogen is dominated by the adsorbed phase pathway and limited by association to the pore (step 2), hence a larger pore has little effect. Hydrogen permeation, on the other hand, is dominated by the gas phase pathway and has the expected linear increase with the pore area.

Figure 7 shows the results for the full multicomponent model predictions for the separation of an equimolar mixture of hydrogen and nitrogen for all six model pores depicted in Figure 6. For the smallest pore, (a), the separation favors hydrogen because of the high energy barrier for passing through the membrane (step 3). However, for larger pores, nitrogen is favored over the smaller hydrogen, because the nitrogen absorbs more strongly to the graphene surface. Furthermore, for the larger pores, (c) through (f), the absolute permeation rates are relatively constant. This is because the molecules no longer experience a significant energy barrier for passing through the plane of the membrane

(step 3), but they still experience a relatively constant energy barrier for entering the pore (step 2) and/or leaving pore (step 4), as shown in Table 3.



**Figure 7:** (a) Predicted mixture separation factors from full numerical computation and (b) total permeation rates for a hydrogen/nitrogen separation using the six model pores depicted in **Figure 6**. Permeation rates and according separation factors are the sum of the gas phase permeation, calculated using equation (2.2), and the permeation from the adsorbed phase pathway calculated from the multicomponent numerical solution of the to the process described by Table 2. Modeled equimolar mixture of hydrogen and nitrogen with  $T=298$  K, total upstream pressure set at 2 atm, downstream set as vacuum.

### 2.2.6 Implications

The gas phase pathway, in which a molecule in the gas phase strikes the pore, is perhaps the more intuitive mechanism for transport through a graphene membrane. However, the adsorbed phase pathway has some important implications on the performance of graphene membranes.

One implication is that the permeation rate, while linear at low pressures, may not be so at pressures high enough to saturate the surface. For the adsorbed phase pathway, the permeation rate in the expected limits becomes independent of pressure at higher pressures. In addition at higher pressures, the pores may be saturated with adsorbed molecules that block gas phase molecules incident on the pore. Potentially, there could be an upper limit to permeation rate; however unaccounted for effects, such as coverage over a monolayer, may somewhat alter such simple behavior at high pressures.

Another important implication of the adsorbed phase model is that the observed permeation rate of a given species is influenced by the partial pressures of all the components of the mixture. This is in contrast to the gas phase pathway, in which the permeation rate for a given species is only dependent on its own partial pressure. This distinction can provide a simple fingerprint for identifying whether or not the adsorbed phase pathway is a significant in future experimental graphene membranes. Even gas phase molecules that are too large to pass through the pores in the membrane can adsorb to the surface and alter the permeation rate of smaller species.

Which path dominates depends on the adsorption characteristics of the gases and the energy barrier of the pores. Smaller pores with higher energy barriers are most likely to give high separation factors. Because a molecule in the adsorbed phase starts at a lower potential energy, the height of the energy barrier it must overcome is necessarily greater than that of a molecule in the gas phase. This makes smaller pores with high energy barriers to be more likely dominated by the gas phase pathway. However, the adsorbed phase still plays a role by blocking the pore from incident gas phase molecules.

Larger pores are more likely to have smaller energy barriers that enable the adsorbed phase to contribute significantly to permeation. Though for large enough pores, it is less likely that the adsorbed phase will block the pore, so both pathways will be present. Depending on the graphene synthesis and membrane fabrication techniques, experimental graphene membranes may have a distribution of different pore sizes. Of the early experimental realizations of SLG and few layer graphene membranes, one is thought to be dominated by small, sub-nm, UV-induced oxidative etched pores;<sup>32</sup> while another is thought to have intrinsic pores over a range of sizes, 1-15 nm.<sup>46</sup> In general, the pathway having the least mass transfer resistance will dominate, but the modeling included in this chapter allows for a combination of adsorbed phase and gas phase dominance when the respective pore populations are balanced.

## 2.3 Conclusions

A SLG membrane has been shown to be capable of high selectivity and high permeance in a way that is not described by conventional membrane diffusion treatments due to its atomic layer thickness. Instead, we apply a surface science approach to successfully derive analytical expressions for the gas and adsorbed phase fluxes through several classes of model graphene pores under different rate limiting steps. The inclusion of the adsorbed phase portion adds important considerations, including altered behavior for mixtures and pore saturation/blocking. These models provide predictions and limits for future modeling, simulation and experimental work with graphene membranes.

### 3 EXPERIMENTAL METHODS AND ANALYSIS OF STOCHASTIC GRAPHENE GAS TRANSPORT

#### 3.1 Introduction

Applications of membrane separations that take advantage of graphene's one atomic layer thickness and regular lattice structure are an emerging area of research. Pristine single layer graphene is impermeable to even the smallest of gases,<sup>7</sup> though recent work has shown there is a mechanism for proton transport.<sup>8</sup> However, by opening well defined pores in the graphene lattice, large separation factors can be achieved. The atomic thickness of the graphene layer is the optimal limit for absolute permeation rate, which is typically limited by the thickness of the membrane material. A variety of simulations and calculations have looked at separations of gas<sup>9-23</sup> and liquid<sup>24-29</sup> systems. However, experimental and theoretical analyses of gas phase transport through isolated graphene nanopores have been few in the literature. In this work, we develop a mathematical formalism that allows one to detect and analyze stochastic gas phase fluxes from graphene membranes, extracting activation energies of pore rearrangements, and even identifying contributions from multiple, isolated pores.

There have been a few experimental demonstrations of membrane systems from single or few layer graphene have been realized. A study by the Bunch group showed that pores created by UV ozone etching in mechanically exfoliated graphene suspended over microcavities in silicon and demonstrating molecular sieving, creating high selectivities

between gas species of differing molecular size.<sup>32</sup> Work using the intrinsic defects in CVD grown graphene transferred onto polycarbonate track etched membranes in aqueous systems was able to demonstrate modest separation of larger molecules and investigated layer stacking to reduce the leakage through those intrinsic defects.<sup>46, 47</sup> Other work with the aqueous phase used a contact seal between a micron scale pipet tip and graphene at the air-water interface to measure conductivity through CVD graphene.<sup>48</sup> Another study used focused ion beam to create pore size distributions centered on multiple sizes from 8 nm to 1  $\mu\text{m}$  in two stacked layers of CVD grown graphene, transferred to and supported on a  $\text{SiN}_x$  membrane, and demonstrated Knudsen selectivity based on the square root of molecular weight typical of classical effusion.<sup>49</sup>

The Bunch group's demonstration of molecular sieving<sup>32</sup> and investigation of mechanical properties<sup>20</sup> uses mechanically exfoliated graphene suspended over a microcavities in a silicon wafer to form a membrane between the gas trapped in the microcavity and the atmosphere; measuring the deflection of the graphene surface over time is used to track the transport of gas. While this technique is not scalable, it does offer the unique advantage of being able to measure the transport characteristics of a single or few subnanometer pores, giving a window towards the fundamental transport characteristics of graphene. Recent work with this platform demonstrates switchable gating of the transport by gold nanoclusters on the graphene membrane surface, as well as smaller but significant fluctuations in transport without gold nanoclusters present<sup>45</sup>.

In this chapter, we present the first mathematical analysis of stochastic gas permeation through any membrane/nanopore system. The model is validated using



experimental results from single layer graphene membranes under batch depletion conditions parametric in starting pressure for He, H<sub>2</sub>, Ne, and CO<sub>2</sub> between 100 and 670 kPa.<sup>45</sup> The model enables one to use membrane deflection curves parametric in starting pressure to confirm a time dependent membrane permeance (pressure normalized molecular flow).

### 3.2 Experimental Methods

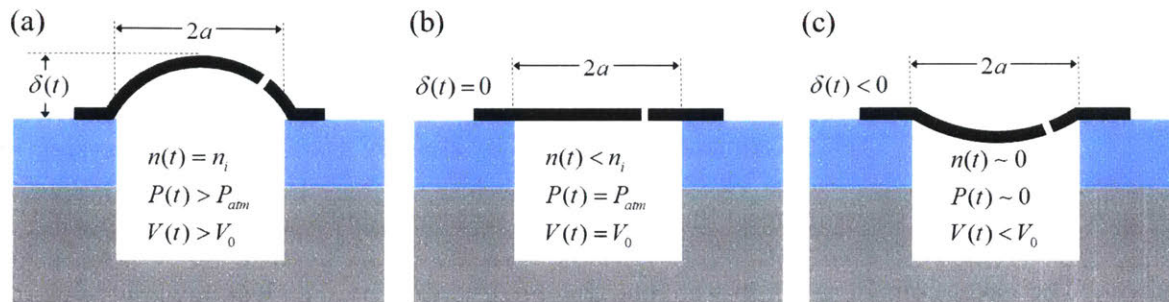
The experimental data for this analysis was collected by the Bunch group on the same device as presented in associated work by the Bunch group,<sup>45</sup> and is an extension of previous methods.<sup>20, 32</sup> In summary, microcavities approximately 800nm deep and 5  $\mu$ m in diameter are formed in grid an oxidized silicon wafer by reactive ion etching, and mechanically exfoliated graphene is deposited on top. Regions of monolayer or bilayer graphene are identified optically and by Raman spectroscopy. The graphene effectively isolates the microcavities from atmosphere, but with diffusion through the silicon dioxide surface, the cavity will equilibrate with their surroundings over the course of days. By placing the sample in a vacuum or pressurized chamber, specific gases can be removed or added to the microcavity at the given pressure. For a pressurized sample, after removing from the pressurized chamber, atomic force microscopy (AFM) measurements show an upward deflection in the graphene surface above a chosen microcavity from the difference between the pressure inside the microcavity and atmospheric. Likewise, the graphene surface deflects downward after being removed from a vacuum chamber. To form a pore, the sample is exposed ultraviolet induced oxidative etching in 30-second or 45-second intervals. Before exposure, the sample is pressurized with H<sub>2</sub> gas, giving an upwards deflection. Between etching exposures, the sample was checked with AFM to

check if the deflection had changed significantly, indicating a pore formation event somewhere in the graphene covering the microcavity. Once a pore forms, the deflection starts to change rapidly and etching is typically ceased. After the etching and pore formation, the microcavity pressurizes and deflates much more rapidly, over the course of minutes to hours depending on the gas species used. The sample can then be repeatedly pressurized and its deflation over time measured with AFM in order to study the transport characteristics through the pore(s) formed. The initial pressurization corresponding to the deflection at the start of AFM measurements ranged from 100 to 670 kPa, with the upper bound limited to avoid delamination of the graphene from the surface, as seen in previous work.<sup>20</sup> The delay between removing the sample from the pressure chamber and AFM measurement was typically around 5 minutes.

### **3.3 Results and Discussion**

#### **3.3.1 Analysis of AFM Membrane Deflection Curves**

Figure 8 illustrates the typical course of an experimental run, in which the deflection of a graphene membrane over a pressurized microcavity is monitored with atomic force microscopy (AFM). The measured deflection can be correlated to the state of the microcavity defined in terms of the mols of gas, pressure, and volume enclosed by the graphene. As shown in Figure 8c, the graphene is typically deflected downwards at the end of an experiment with smaller gases because the air gases enter much more slowly than the charged gas evacuates the microcavity. Data from two different samples is presented here: sample 1 was formed with a suspended single layer of graphene and sample 2 was formed with a suspended bilayer of graphene.



**Figure 8.** Depiction of experimental system depicting microcavity in Si/SiO<sub>2</sub> (grey/blue) covered by a single layer graphene membrane (black bar) with randomly located pore(s) represented by a break in the black bar. Illustrations are labeled with variables as used in models;  $a$  for microcavity radius,  $\delta$  for membrane deflection,  $n$  for mols of gas in microcavity,  $P$  for internal microcavity pressure, and  $V$  for microcavity volume enclosed by graphene. Panes depict variation over course of typical experimental run (a) at the start, (b) in the middle at zero deflection, and (c) at the end. Reprinted with permission from *Drahushuk, L.W. et al. ACS Nano 10, 786-95 (2015)*. Copyright 2015 American Chemical Society.<sup>66</sup>

From mechanical models of thin films, the pressure within the cavity can be related to the observed deflection ( $\delta$ ) according to the following relation,<sup>67</sup>

$$P(\delta(t)) = \frac{EwK(v)}{a^4} \delta(t)^3 + \frac{4S_0}{a^2} \delta(t) + P_{atm} \quad (3.1)$$

where  $E = 1$  TPa is the Young's modulus,  $w = 0.34$  nm is the film thickness,  $K(v) = 3.09$  is a constant determined by Hencky's solution and the system geometry,  $S_0 = 0.1$  N/m is the initial surface tension, and  $a$  is the well radius.<sup>20</sup> The thickness and Young's modulus of single layer graphene are not precisely defined; however, the reported values fit deflection data collected at known pressures. Similarly, the volume of the microcavity can be described by,

$$V(\delta(t)) = C(v) a^2 \pi \delta(t) + V_0 \quad (3.2)$$

where  $C(v) = 3.09$  is a constant determined by Hencky's solution and the system geometry, and  $V_0$  is the volume of the microcavity with zero deflection of the graphene sheet. The gases considered in this chapter can be described by the ideal gas law, as shown in equation (3.3), but our results easily extend to more complex equations of state.

$$n(t) = \frac{P(\delta(t))V(\delta(t))}{RT} \quad (3.3)$$

Here,  $n$  is the mols of gas,  $P$  is the microcavity absolute pressure,  $V$  is the microcavity volume,  $T$  is the temperature, and  $R$  is the ideal gas constant. A mass balance on the permeating gas relates the rate of change of enclosed gas ( $dn/dt$ ) to the sum of the gas flow(s) through the pore(s),  $\dot{n}_{pore}$ , and the leakage through the microcavity edges,  $\dot{n}_{background}$ . Previous work has shown that the molar flow through the pore is one to several orders of magnitude larger than the background leakage depending on the gas, based on comparing results before and after etching and pore formation<sup>45</sup>; therefore we will treat  $\dot{n}_{background}$  as negligible in subsequent analysis, as summarized in equation (3.4).

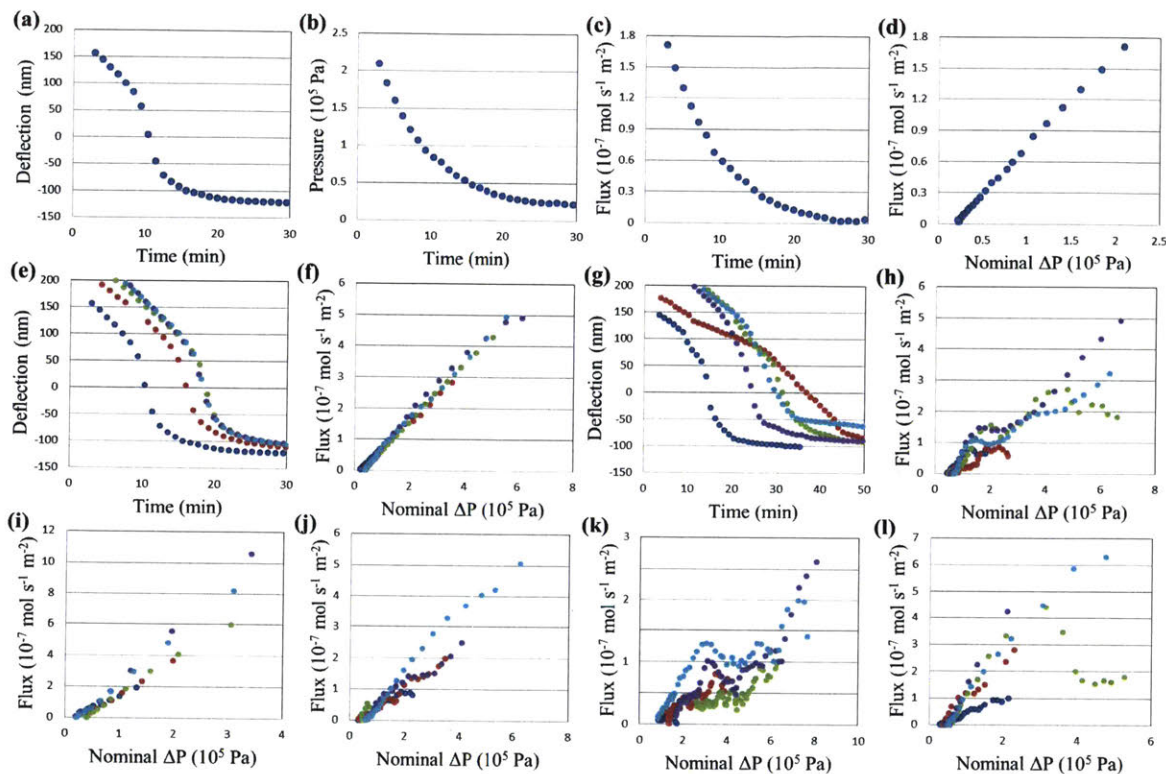
$$\frac{dn(t)}{dt} = \dot{n}_{pore}(t) + \dot{n}_{background}(t) \approx \dot{n}_{pore}(t) \quad (3.4)$$

In order to obtain a value for the gas flow ( $dn/dt$ ) out of the chamber, the differential is applied to equation (3.3), with the dependence of pressure and volume on deflection emphasized.

$$\frac{dn(t)}{dt} = \frac{1}{RT} \frac{d\delta(t)}{dt} \frac{d(P(\delta)V(\delta))}{d\delta} \quad (3.5)$$

Equation (3.5) provides a method to use the slope of the measured deflection *versus* time to extract the instantaneous flow of gas out of the etched pore as a function of pressure. For this chapter, we used a rearrangement of this equation that enabled extracting values from the data using a linear least squares fit.<sup>45</sup> With these relations, we follow the permeation behavior of the gas over the time just from the AFM measurements of deflection *versus* time.

Figure 9a-d demonstrates the use of the relations for a single experimental run with He gas. The experimental deflection data in Figure 9a is used to calculate the pressure and flux, molar flow normalized by membrane area, in b and c at each time point. Equation (3.5) can be utilized to investigate the transport mechanism by examining the dependence of the flux *versus* pressure, as done in Figure 9d, corresponding to the data in Figure 9a. This plot of flux *versus* pressure difference can help confirm the primary mechanism of gas permeation. The linearity of plot Figure 9d, for example, is consistent with nanopore transport (effusion) or Knudsen diffusion through the pore. Nanopore transport with molecular sieving is confirmed as the mechanism by showing that the ratio of permeance values exceeds Knudsen selectivities, which are determined by the inverse square root of molecular weight ratio for the series of gases.<sup>45</sup> The linearity rules out Poiseuille flow through a larger orifice which would demonstrate a quadratic dependence on pressure.



**Figure 9.** (a) Measured deflection *versus* time, (b) calculated microcavity pressure *versus* time (c) calculated gas flux *versus* time, and (d) flux *versus* driving pressure difference for He transport with an initially observed pressure of 210 kPa (absolute). (e) Measured deflection *versus* time and (f) flux *versus* pressure difference for five sets of He experiments with initial pressures in the range 210 to 555 kPa; demonstrates expected linear behavior for flux *versus* pressure. (g) Measured deflection *versus* time and (h) flux *versus* pressure difference for five sets of  $H_2$  experiments with initial pressures in the range 100 to 670 kPa; demonstrates some deviations from the general expected linear behavior for flux *versus* pressure. (a)-(h) represent data collected from sample 1, a single layer graphene device. Flux *versus* pressure difference for (i) He, (j)  $H_2$ , (k) Ne, and (l)  $CO_2$  were collected with sample 2, a bilayer graphene device. Reprinted with permission from Drahushuk, L.W. *et al. ACS Nano* 10, 786-95 (2015). Copyright 2015 American Chemical Society.<sup>66</sup>

Furthermore, for the same membrane, the correlation between flux and pressure difference should be identical for all experiments. This is exactly what is seen in Figure 9f, a collection of five experiments for He. For the five experiments of H<sub>2</sub> in Figure 9h, however, the curves for the each experiment do not overlap perfectly with another; and there are seemingly random divergences from perfect linearity, even if the general trend is still linear. These divergences appear stochastic, and are uncorrelated to pressure or mechanical position of the graphene. In considering the reason for these divergences, we first consider the corresponding measured deflection data used to calculate flux, show in Figure 9e and g.

In Figure 9e, the deflection curves are all self-similar, which we define as having identical functional dependences translated along time axis according to the initial pressure only. In gas transport theory, the rate of isothermal transport is a function of the chemical potential difference across the pore, which simplifies to the partial pressure difference for low to moderate total pressure. Note that even for a strongly adsorbing gas, the transport rate is a function of pressure only under these conditions (related through the adsorption isotherm). Figure 9g gives examples of deflection data for H<sub>2</sub> that is not self-similar, which we will explore in the following section.

### 3.3.2 A Mathematical Interpretation of Intersecting Deflection Curves

In understanding Figure 9e, it is useful to consider the following mathematical derivation, which shows that deviations from self-similarity in these curves mean that the transport rate is varying temporally, independently of pressure. We define a generic

pressure dependence of a single component molar flow,  $f(P)$ , across the pore such that the differential equation describing the deflating microcavity system becomes:

$$\frac{dn}{dt} = f(P) \quad (3.6)$$

Note that this function encompasses all versions of adsorption and diffusion models possible for the membrane system, and incorporates all possible rate limiting steps from our previous analytical work.<sup>14</sup> Re-writing equation (3.6) in terms of the deflection via the idea gas law yields equation (3.7).

$$\frac{dn}{dt} = \frac{1}{RT} \frac{d\delta}{dt} \frac{d(P(\delta)V(\delta))}{d\delta} = f(P(\delta)) \quad (3.7)$$

Note that this generic form remains separable such that upon integration:

$$\int_{\delta_0}^{\delta} \frac{1}{f(P(\delta))RT} \frac{d(P(\delta)V(\delta))}{d\delta} d\delta = \int_0^t dt \quad (3.8)$$

Defining the solution of the left integral as a generic function  $G(\delta)$  we find that,

$$G(\delta) - G(\delta_0) = t \quad (3.9)$$

Applying the inverse of the generic function,

$$\delta = G^{-1}(t + G(\delta_0)) \quad (3.10)$$

The functional form of equation (3.10) describes curves of deflection *versus* time that are identical except for a shift in along the time axis given by the constant  $G(\delta_0)$ ,



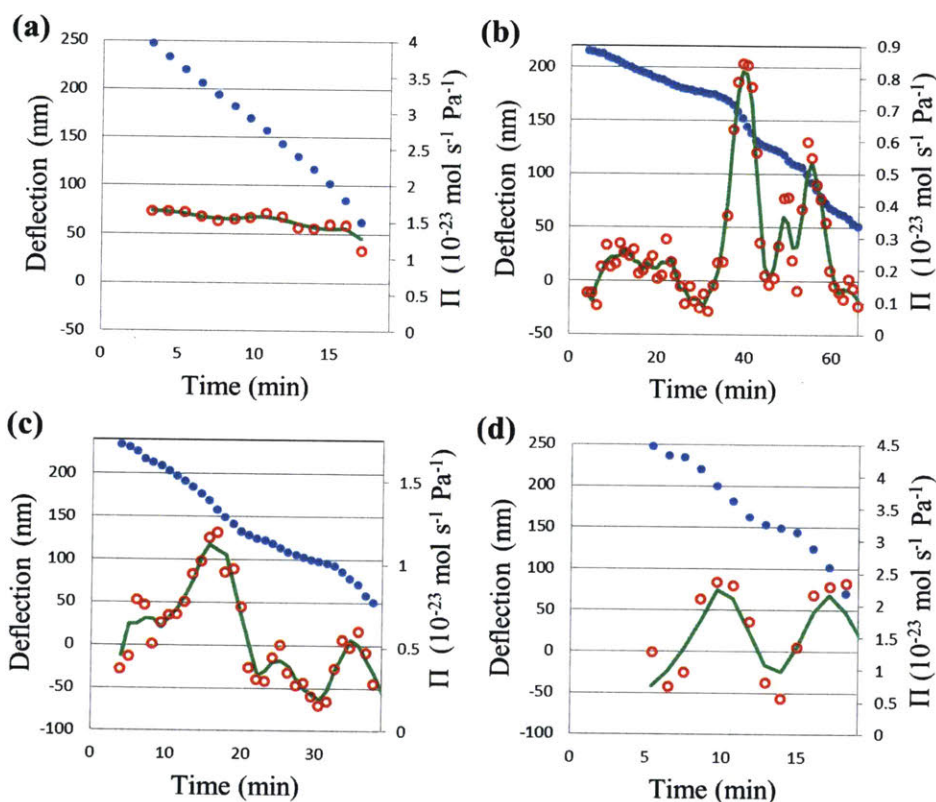
which is a function of the initial pressure, and matches the definition for self-similarity. This is indeed the case for He, shown in Figure 9d, with a corresponding linearity between flux and pressure that reveals a constant, time invariant slope, as predicted by equation (3.10). It then follows that the departure from self-similarity in Figure 9g means that  $f(P, t)$ , or that the transport of gas has some time dependence (the only remaining dependent variable) outside of the expected pressure dependence. Hence, we take the intersecting deflection curves to imply:

$$\frac{dn}{dt} = \Pi(t) \Delta P \quad (3.11)$$

We consider the flow of gas in terms of what we define as the membrane permeance, with the molar rate normalized by the pressure difference. A typical membrane will have a constant permeance, corresponding to a linear molar flow with pressure. To account for the time dependent behavior of the transport, we modify our expectation of the molar flow rate,  $dn/dt$ , so that it includes a time dependent permeance,  $\Pi(t)$ , for cases where self-similarity does not appear to be observed.

For the case of He, with its self-similar deflection curves, the permeance,  $\Pi(t)$ , remains essentially constant with time. However, the permeances for other data sets, H<sub>2</sub>, Ne, and CO<sub>2</sub>, show obvious variation in time. Figure 10 shows a few examples of the variation in permeance with time, plotted alongside the experimentally measured deflection curves. Figure 10a, an example data set for an experimental run with He shows that the permeance remains mostly constant. In the other panels, there are sharp changes that occur at various times. These are discrete changes in the values permeance

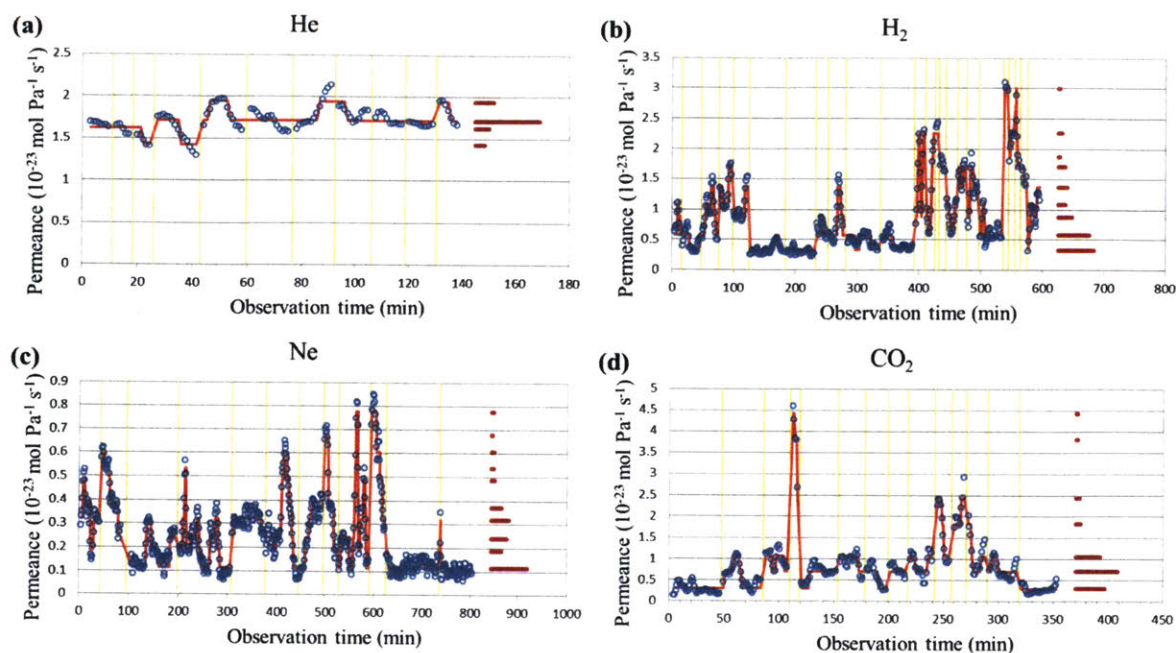
and correspond to kinks and changes in slope of the deflection curves. They typically appear smoothed even though the changes are discrete because the fitting method used to extract the permeance values must fit the slope across multiple points; Figure 10 shows two levels of smoothing, red dots with low smoothing from using only three points to extract permeance, and a green line with more smoothing using five points in the extraction.



**Figure 10.** Deflection (blue closed circles) and permeance (red open circles) *versus* time over experiment for examples runs with (a) He, (b) Ne, (c) CO<sub>2</sub>, and (d) H<sub>2</sub> with sample 1. The green line is a smoother fit of permeance, using additional points when fitting the slope. Demonstrates that kinks and changes in slope in the measured deflection that are indicative the corresponding changes in permeance. Adapted with permission from *Drahushuk, L.W. et al. ACS Nano 10, 786-95 (2015)*. Copyright 2015 American Chemical Society.<sup>66</sup>

### 3.3.3 Hidden Markov Analysis of Time Dependent Permeance

Each individual experimental run is isolated by the preparatory step of re-pressurizing the microcavity. However, all experiments are performed on the same membrane, and therefore, we assume that the observed transport properties are consistent across all experimental runs for a given gas. To visualize trends, we have concatenated the data from each run with that gas species into a single time axis referred to as “observation time” in Figure 11. We included only data points corresponding to measured deflections above 50 nm, as points at low deflections were more sensitive to experimental error; and permeance was extracted by using five data points, equivalent to the green line of Figure 10. To help analyze and fit the data to discrete states, we employed hidden Markov modeling via the program HaMMy.<sup>68</sup> This fits the permeance data to up to ten discrete states with instantaneous transitions between them. Some of these transitions fall at the time points corresponding to breaks between experimental runs, but these transitions were excluded from later quantitative analysis of transition frequency.

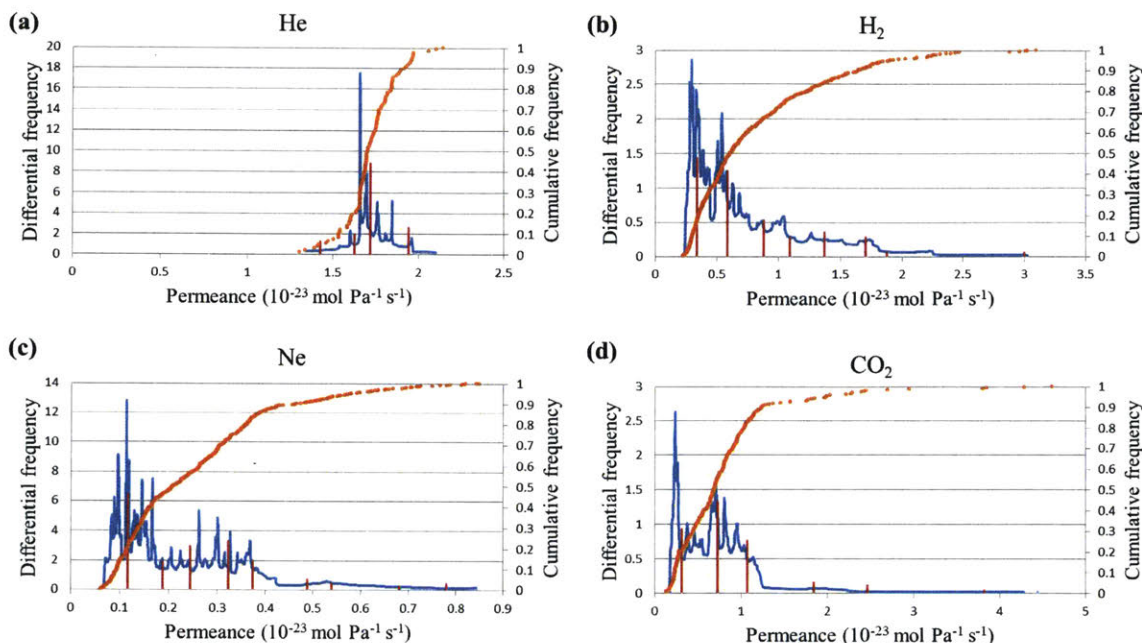


**Figure 11.** Permeance *versus* time for all experiments (blue open circles) concatenated for each of (a) He, (b)  $\text{H}_2$ , (c) Ne, and (d)  $\text{CO}_2$  with sample 1. Red lines represent a hidden Markov model fit to discrete states. Bars in the right of each pane represent time spent in each fitted state. Orange vertical lines mark the transitions where data was merged between different experimental runs. Reprinted with permission from *Drahushuk, L.W. et al. ACS Nano 10, 786-95 (2015)*. Copyright 2015 American Chemical Society.<sup>66</sup>

As an alternate visualization of the states, the derivative of the cumulative frequency of observed permeance values is plotted in Figure 12. All the data points are arranged by permeance to give the cumulative distribution, and taking the derivative yields the differential frequency as the distribution of observed permeance values. This presentation assists in identifying the most commonly occurring states. The temporal information is lost in this presentation, which makes it more difficult to identify rarer that were distinct states in Figure 11, most notably the higher permeances. This plot accurately summarizes the most commonly occurring states. The states from the above



HaMMY fitting are also represented in Figure 12, showing overlap between some though not all of the features appearing in the differential frequency distribution.

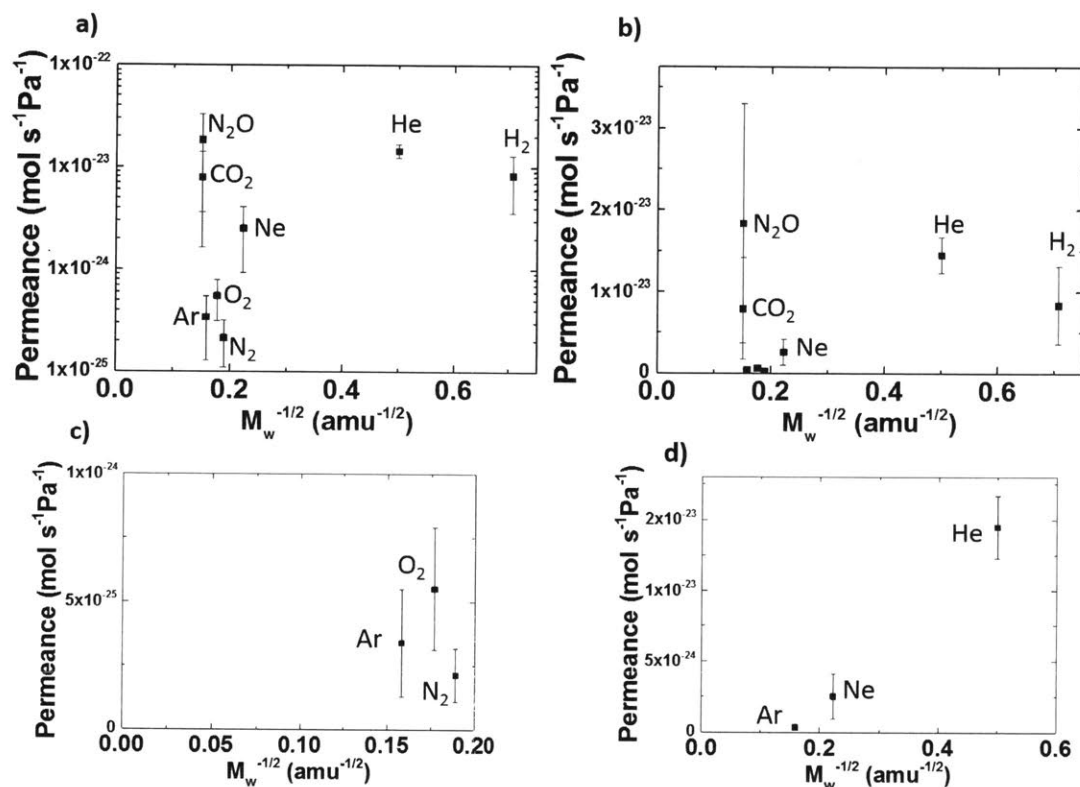


**Figure 12.** Cumulative frequency of observed permeance (orange dots) along right vertical axis, differential frequency (blue line) plotted against left vertical axis, and HaMMY fits from **Figure 11** for each of (a) He, (b) H<sub>2</sub>, (c) Ne, and (d) CO<sub>2</sub>.

### 3.3.4 Evaluation of Average Permeance in Relative to Expected Behavior

Figure 11 and Figure 12 illustrate the variance in the observed permeance over the course of the experimental study, however, some observations can still be made for the relative permeances of the gases to illustrate the transport mechanisms involved. Figure 13 summarizes the permeance results versus the inverse square root of molecular weight to compare to the Knudsen effusion model, including some gases, N<sub>2</sub>O, Ar, O<sub>2</sub>, and N<sub>2</sub>, from work other than that discussed above.<sup>45</sup> Knudsen effusion behavior, described by equation (2.1), has an inverse square root dependence on molecular weight, meaning the

data points would be linear from the origin in Figure 13b-d. The plots show that few, if any, of points would fall on the same line through the origin.



**Figure 13.** (a) Permeance plotted versus the inverse square root of the molecular mass of He, Ne, Ar, H<sub>2</sub>, N<sub>2</sub>O, CO<sub>2</sub>, O<sub>2</sub>, and N<sub>2</sub> in log scale. (b) in linear scale. (c) Permeance versus square root of the molecular mass of Ar, O<sub>2</sub>, and N<sub>2</sub>. (d) Permeance versus square root of the molecular mass of the noble gases. Reprinted with permission from Wang, L. et al. *Nat Nano* 10, 785-90 (2015).<sup>45</sup>

### 3.4 Conclusions

In conclusion, the technique of measuring gas permeance through AFM measured changes in the bulge deflection over time can be used to extract the permeance and the gas transport characteristics. Further, we demonstrated the permeance can be tracked

over time and revealed stochastic and discrete changes among difference states with large changes in permeance. This chapter details the analysis of the first time stochastic state switching has been observed in a gas phase system, and the extraordinary sensitivity of the gas permeance and the localization of the transport at a single point gives this platform potential to be applied to issues of sensing and nanoscale material management, such as “nanoprinting” or nanocatalysis.

## 4 ANALYSIS OF MULTIPLE STOCHASTIC STATES IN FINITE PORE SYSTEM

### 4.1 Introduction

In Figure 11, the data sets corresponding to H<sub>2</sub>, Ne, and CO<sub>2</sub> all show large changes in permeance up to around a factor of ten, and multiple states are observed, with HaMMy fitting between seven and ten states. Many examples of state switching in pores occur as two states, and more observed states are the result of multiple two-state pores. To investigate whether multiple pores could be responsible for the many states observed in Figure 11, we looked at the relations given by the Markov network for a fixed number of pores and applied analysis based on them to the data. With multiple two-state pores, two pores yields four possible observed states, three pores yields eight possible observed states, four yields sixteen possible observed states, and so on. A three pore system has a comparable number of states to those from HaMMy fitting; therefore, our analysis focuses on matching a three pore system.

Stochastic fluctuations of the gas permeance can be analyzed using a Hidden Markov model to fit discrete states and estimate the activation barrier for switching. Our formalism also teaches how to use the relations between the states given by the Markov network for a collection of pores to determine the operative number that describe the data.



## 4.2 Assignment of system to discrete number of pores described by

### Markov Network


















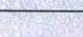
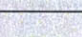
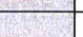






#### 4.2.1 Three pore model

For evaluating goodness of fit for the data discussed in the previous chapter to the three pore model, the constraints imposed on the observed state permeance level and state transitions are what differentiate the alternate hypothesis of fewer than three pores having many states. The first step in evaluating those properties is to describe the system to by eight states, which are determined by four underlying parameters. The eight states correspond to the possible combinations of the two-state pores, which we describe as having “high” and “low” permeance states. How well the data can be fit by these four parameters can be one test of the three pore hypothesis. The relations that describe the eight observed permeance states are described by the matrix problem in equation (4.1);  $x$  is the combined permeance of the low states for all three pores;  $y_a$ ,  $y_b$ , and  $y_c$  are the difference between the high and low states for the first, second, and third pores respectively; and  $\Pi_j$  is the permeance value for the  $j$ th observable state.

$$\begin{pmatrix} y_a \\ y_b \\ y_c \end{pmatrix} \begin{pmatrix} 0 & 0 & 0 \\ 1 & 0 & 0 \\ 0 & 1 & 0 \\ 0 & 0 & 1 \\ 1 & 1 & 0 \\ 1 & 0 & 1 \\ 0 & 1 & 1 \\ 1 & 1 & 1 \end{pmatrix} + x = \begin{pmatrix} \Pi_1 \\ \Pi_2 \\ \Pi_3 \\ \Pi_4 \\ \Pi_5 \\ \Pi_6 \\ \Pi_7 \\ \Pi_8 \end{pmatrix} \quad (4.1)$$

With the convention that  $y_a < y_b < y_c$ , the permeance values  $\Pi_j$  in equation (4.1) are always ordered in increasing permeance with the exception of  $\Pi_4$  and  $\Pi_5$ , the order of which should be swapped if  $(y_a + y_b) < y_c$ . Table 5 summarizes the set of relations described by equation (4.1) under the column for observed permeance.

**Table 5.** Summary of nomenclature defined in equations (4.1)-(4.11) with illustrations showing the corresponding pore configurations.

Individual pore					
State	Pore			Individual permeance	Fraction of total time spent in state
“Low”				$x_a$	$(1 - p_a)$
“High”				$x_a + y_a$	$p_a$
Observed states (three pores)					
State	Pores			Observed permeance	Fraction of total time spent in state
	a	b	c		
1				$\Pi_1 = x_a + x_b + x_c = x$	$P_1 = (1 - p_a)(1 - p_b)(1 - p_c)$
2				$\Pi_2 = x + y_a$	$P_2 = p_a(1 - p_b)(1 - p_c)$
3				$\Pi_3 = x + y_b$	$P_3 = (1 - p_a)p_b(1 - p_c)$
4				$\Pi_4 = x + y_c$	$P_4 = (1 - p_a)(1 - p_b)p_c$
5				$\Pi_5 = x + y_a + y_b$	$P_5 = p_a p_b(1 - p_c)$
6				$\Pi_6 = x + y_a + y_c$	$P_6 = p_a(1 - p_b)p_c$
7				$\Pi_7 = x + y_b + y_c$	$P_7 = (1 - p_a)p_b p_c$
8				$\Pi_8 = x + y_a + y_b + y_c$	$P_8 = p_a p_b p_c$

After defining the permeance levels of the states, we move on to look at the dwell times and transitions. Ideally, the statistics of the transitions from state to state can show unique characteristics of a three pore system, however the transitions are more difficult to use as a distinguisher because of the effects of smoothing that occurs from the calculation of permeance from deflection and the fact that the full data set is a concatenation of many shorter, isolated segments of AFM measurements. However, the dwell time, in particular the total time spent in each state, is relatively unaffected by those issues and is useful as a distinguishing measure.

In our analysis, we define the lower case  $p_i$  to be the fraction of time a single pore, in this case pore a, b, or c, spends in its high permeance state, given by equation (4.2), where  $t_i$  is the time spent in the high permeance state of the  $i$ th pore and  $t_{total}$  is the total time. It can also be considered the probability of finding the pore in its high permeance state.

$$p_i = \frac{t_i}{t_{total}} \quad (4.2)$$

$p_i$  as defined by equation (4.2) is an underlying property of an individual pore, related to the thermodynamic equilibrium and free energy difference between the two states; it is not directly related to a single observable state, as the observed states come from a combination of pores; it can be calculated as a sum of observed state times, or from other relations as shown below. We use the capitalized  $P_j$  of equation (4.3) to indicate the fraction of time spent in each observable state, where  $t_j$  is time spent in the  $j$ th observed state from experimental results.

$$P_j = \frac{t_j}{t_{total}} \quad (4.3)$$

The fraction of time in each of the eight observable states, the eight  $P_j$ , should be related to the probabilities the individual pores are in their high permeance states. The relations are described by equations (4.4)-(4.11) and are also summarized in Table 5 under the column for fraction of time spent in state.

$$P_1 = P_{000} = (1 - p_a)(1 - p_b)(1 - p_c) \quad (4.4)$$

$$P_2 = P_{100} = p_a(1 - p_b)(1 - p_c) \quad (4.5)$$

$$P_3 = P_{010} = (1 - p_a)p_b(1 - p_c) \quad (4.6)$$

$$P_4 = P_{001} = (1 - p_a)(1 - p_b)p_c \quad (4.7)$$

$$P_5 = P_{110} = p_a p_b(1 - p_c) \quad (4.8)$$

$$P_6 = P_{101} = p_a(1 - p_b)p_c \quad (4.9)$$

$$P_7 = P_{011} = (1 - p_a)p_b p_c \quad (4.10)$$

$$P_8 = P_{111} = p_a p_b p_c \quad (4.11)$$

From equations (4.4)-(4.11), the probability that each of the pores is in the high state ( $p_a$ ,  $p_b$  and  $p_c$ ) can be found by solving the system of non-linear equations for these

three variables, as done below. These parameters are related to four of the  $P_j$  values analytically via:

$$p_a = \frac{P_8}{P_7 + P_8} \quad (4.12)$$

$$p_b = \frac{P_8}{P_6 + P_8} \quad (4.13)$$

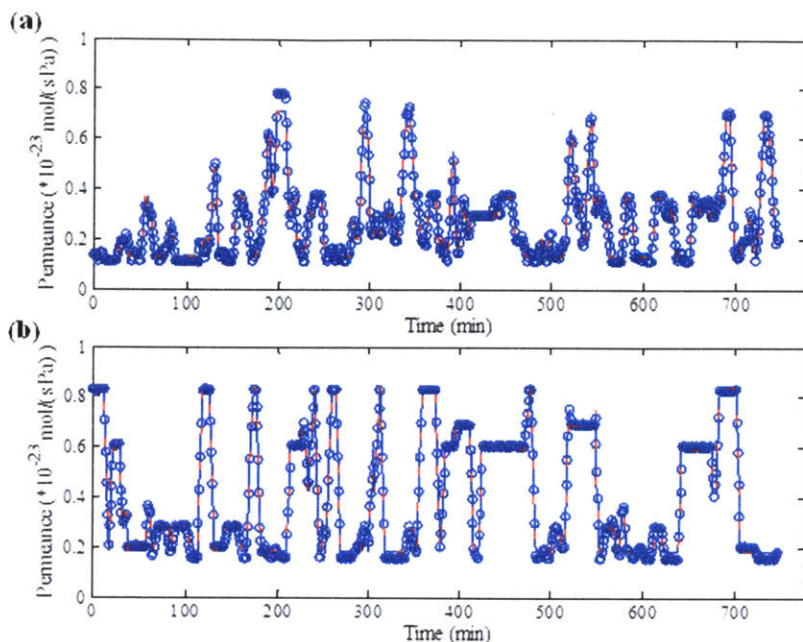
$$p_c = \frac{(P_6 + P_8)(P_7 + P_8)}{P_8} \quad (4.14)$$

### 4.3 Comparison to simulated data sets

Going further in order to establish confidence in assignment to a three pore system, we used a Monte Carlo approach to generate simulated data in the form of the experimentally obtained permeance *versus* time. First we simulated data corresponding to three independent pores, as described by the equations of the previous section, summarized in Table 5; we refer to these as “positive simulations.” At each fixed time step, each of the three pores had a given probability of changing its state from high to low, or low to high. The probabilities of both those transitions are distinct, meaning six probabilities are used to control the transitions to and average time spent in each state. In addition to six probabilities, a variable for each of the three pores,  $y_a$ ,  $y_b$ , and  $y_c$ , describes the difference between that pore’s high and low permeance states, and the overall lowest observed permeance state,  $x$ , is described by a single variable. With values for these parameters, we simulated permeance *versus* time points for the same number of time points as the experimental data set. The data was smoothed by averaging the four closest

points in time to emulate the smoothing that results from the calculation of permeance from experimentally measured deflection of graphene over the microcavity. A small amount of random Gaussian noise is also added to the simulated permeance data set. The total number of simulated data points was set to 700 to match the size of the experimental Ne data set, as the size of the data set is an important factor in the level of confidence that can be achieved. Figure 14a shows an example simulated data set generated with the three pore model.

For the case of three independent pores, the observed permeance levels and state probabilities are constrained by the relations in equations (4.1) and (4.4)-(4.11) and determined by the hidden parameters for the three pores; in a system with eight uncorrelated states, the observed states would not be bound by those relations. In an equivalent manner as the previous described positive simulations case, alternate simulations were carried out such there were eight states with independent parameters, unconstrained by the relations of a three pore system; we refer to such simulations as “negative simulations.” The resulting simulated data sets were qualitatively similar the experimentally obtained permeance *versus* time. Figure 14b gives an example data set from a negative simulation. To test the hypothesis and evaluate the confidence in assigning the experimental system as three pore, we performed 450 negative simulations with eight states not constrained to a three pore system and 150 simulations of a model three pore system. These sets of simulations were generated with parameters that would result in data qualitatively similar to the experimental data in terms of the frequency of transitions; full details of parameters of simulations can be found in the supporting information.



**Figure 14.** (a) Example simulated data set generated using three pore model, positive simulation. (b) Example simulated data set generated with eight states unconstrained by three pore model relations, negative simulation.

### 4.3.1 Simulation procedures

The positive simulations were generated with the three pore model and a set of parameters to give data sets qualitatively similar to the experimental data sets. At each time step, each of the pore in the “low” permeance state had a probability of randomly switching to the “high” permeance state, and each pore in its high permeance state had a distinct probably of randomly switching to its low permeance state. Once the pores are given a chance of switching states, the output permeance value is a sum of the low permeance states, plus the difference between the high and low permeance states for any pores in the high states, as summarized in Table 5. The probabilities for switching states, and the permeance difference between the high and low states are given in Table 6. The sum of the low states in these simulations was  $0.109 \times 10^{-23}$  mol s<sup>-1</sup> Pa<sup>-1</sup>. This process was

repeated for each time point to generate data that adheres to the three pore model. Once the data at each point was generated, the permeance value of each point was averaged with its two nearest neighbors, both before and after the point, to emulate the smoothing that results from fitting in the experimental data; a small amount of random normal noise, standard deviation  $0.002 \times 10^{-23} \text{ mol s}^{-1} \text{ Pa}^{-1}$ , was also added to each smoothed data point. The purpose of these simulations was to determine the how well a data set of limited size would conform to the relations of the three pore model.

**Table 6.** Simulation parameters for positive simulations following the three pore model.

Pore	Probability of switching to “high” permeance state at time step	Probability of switching to “low” permeance state at time step	Permeance difference between “high” and “low” states ( $10^{-23} \text{ mol s}^{-1} \text{ Pa}^{-1}$ )
a	0.13296	0.01911	0.0829
b	0.06575	0.10354	0.1814
c	0.01191	0.08037	0.4042

Data sets from negative simulations were generated in a very similar manner as with the positive simulations. In these simulations, the system was given a probability to leave its current state at a given time step, and then could enter any of the other seven states. The relative probabilities and permeance values for the eight states were all distinct, and their averages were given by

Table 7. When in use, the relative probabilities were renormalized to a sum of one. For the probability of entering the state, and the permeance value of the state, the parameters between simulation runs varied by a multiplier centered at one with normal random deviation with standard deviations of 0.11 and 0.03 respectively. The probabilities of



leaving a state were varied from state to state and across simulation runs according to equation (4.15), where  $M$  was a constant corresponding to the average probability of leaving the state and  $r$  was a normal random number centered about zero with a standard deviation of 4.

$$\text{probability of leaving state} = \frac{2}{(1+r+M)} \quad (4.15)$$

At each time point, the current state's probability of leaving determined the random chance of leaving that state and transitioning to a new one; if leaving the state, the probabilities for entering the other seven states were renormalized to a sum of 1 and one state was randomly chosen, weighted by the probabilities, for the new time point. This procedure was repeated for each time point in simulated data set. Parameters were randomized as described above between simulated data sets. Data points were smoothed with averaging and a small amount of random noise was added in the same manner as described above for positive simulations. The parameters for negative simulations were randomly varied because the purpose of negative simulations was to determine the likelihood that a data set of limited size that was not generated as a three pore system could be fit well to the constraints and modeling of a three pore system.

**Table 7.** Average simulation parameters for randomized parameters in negative simulations having eight states unconstrained by the relations defining the three pore model. The relative probabilities of the entering a state were renormalized to a sum of one when used in simulations.

State	Average relative probability of entering state upon leaving another	Average probability of leaving state at time step	Permeance value of state ( $10^{-23} \text{ mol s}^{-1} \text{ Pa}^{-1}$ )

1	0.3	0.0952	0.1000
2	0.25	0.1111	0.2143
3	0.2	0.1429	0.3286
4	0.15	0.1818	0.4429
5	0.09	0.1333	0.5571
6	0.05	0.1000	0.6714
7	0.08	0.1538	0.7857
8	0.05	0.1818	0.9000

### 4.3.2 Analysis of Goodness of Fit of Data Sets

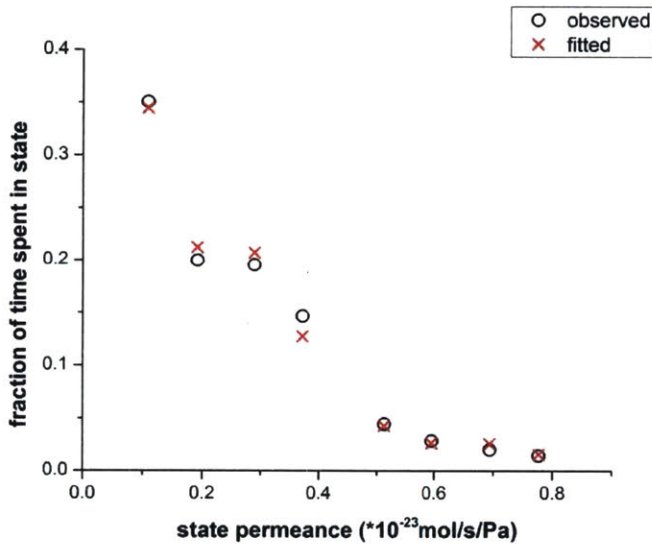
For analyzing either the experimental data sets or simulated data, the data set was fit with a least squares approach to the eight states using the definition of sum squared error,  $SSE_{\Pi}$ , defined by equation (4.16), where  $N$  is the total number of permeance data points,  $\Pi(t_k)$  is the permeance value at a given time point  $t_k$ , and the set of  $\Pi_j(x, y_a, y_b, y_c)$  are the model permeance states defined by equation (4.1).

$$SSE_{\Pi} = \sum_{k=1}^N \min_{j=1-8} \left\{ \left( \Pi(t_k) - \Pi_j(x, y_a, y_b, y_c) \right)^2 \right\} \quad (4.16)$$

After fitting permeance data points to the model states as described above, we then assigned each point to a given state and calculated fraction of time spent in each observed state,  $P_j$  as described in equation (4.3). To provide a measure of the goodness of fit to three pores, we then applied a second least squares fit on the eight values of time spent in each state,  $P_j$ . The sum of squared error for this fit,  $SSE_P$ , is described in equation (4.17),

$$SSE_P = \sum_{j=1}^8 \left( P_{j,obs} - P_j(p_a, p_b, p_c) \right)^2 \quad (4.17)$$

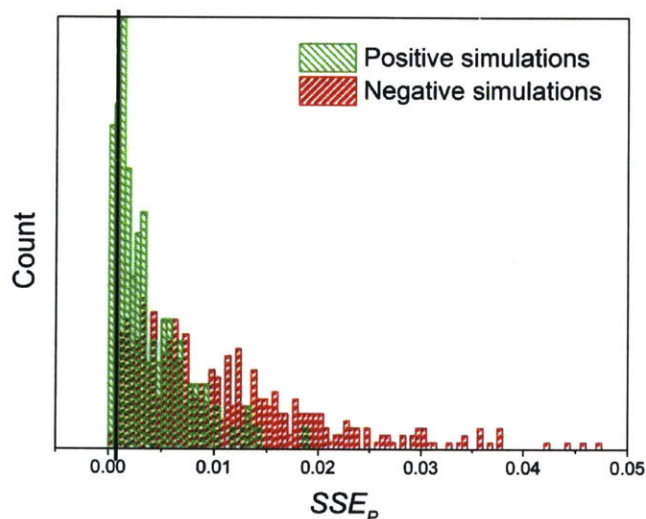
where  $P_{j,obs}$  is the value calculated directly from the data set and  $P_j(p_a, p_b, p_c)$  is the value calculated appropriate expression in equations (4.4)-(4.11), with  $p_a$ ,  $p_b$ , and  $p_c$  varied as parameters for the least squares optimization. Figure 15 illustrates this fitting for the case of the Ne data set studied; the fitted values are summarized in Table 8.



**Figure 15.** Comparison of the values for fraction time spent,  $P_i$ , between the observed values from the experimental results and the values calculated from the three fitted parameters of the three two-state pores model in equations (4.4)-(4.11).

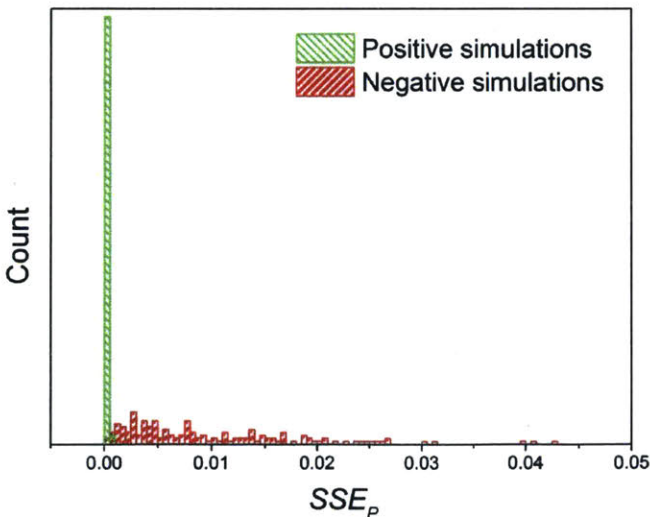
The sum of squared error for this fit,  $SSE_P$  from equation (4.17), provides a measure for the goodness of fit to three pores; there are eight values of fraction time spent for the eight observed states fitted with least squares using three parameters. We preferred this distinguisher when comparing the analysis between simulation and experimental results, as it is less sensitive to the magnitude of noise in the permeance values. The histogram in Figure 16 compares the distribution of  $SSE_P$  values between the positively and negatively generated data sets, as well as marks the experimental value for

the Ne data sets with a vertical line. There is significant overlap between the two sets, meaning distinguishing between the two is often difficult data sets of this size, however, the evaluation of the  $SSE_p$  for the experimental data shows that it can be distinguished in this case. The experimental data set for Ne lies at the 15<sup>th</sup> percentile for positive simulations of the same number of data points as collected for Ne, placing them within the typical range of simulations. For the negative simulations, not generated with a three pore model, the experimental results were at the 1<sup>st</sup> percentile, being a better fit than nearly all of the simulated data sets. This allows us to place a high degree of confidence in our statement that the experimental sample is consistent with a three pore system.



**Figure 16.** Histogram of the sum squared errors ( $SSE_p$ ) when fitting fraction of time spent to three pore model. Positive simulations (green) are generated by a mock three pore system; negative simulations (red) are generated with randomized parameters for eight states unconstrained by three pore relations. The vertical black line represents locations of experimental results for Ne with sample 1. Reprinted with permission from *Drahushuk, L.W. et al. ACS Nano 10, 786-95 (2015)*. Copyright 2015 American Chemical Society.<sup>66</sup>

Additional simulations summarized in the Figure 17 of the supplementary information show that the overlap and spread of the positive simulations results from the finite size of the data set and the smoothing/noise inherent to the analysis of the experimental data or intentionally added in simulations. These simulations were performed with the same parameters as those in Figure 16 but with a much greater number of simulated data points, 7000 instead of 700, and without added smoothing. Increasing the number of data points averages out the stochastic nature of the fluctuations and makes the observed values more consistent with the ideal relations defined in the main text. These simulations served to confirm that the “positive” simulations fit to the three pore model and that “negative” simulations are not accurately fit by the model by removing the other factors, small data sets and smoothing. Figure 17 gives the distribution of  $SSE_p$ , defined in equation (4.17), for these simulations; it is consistent with expectations, in that the positive simulations can be fit near perfectly (sum squared error near zero), and the distinction between the positive and negative sets is much clearer.



**Figure 17.** Histogram of the sum squared errors ( $SSE_p$ ) when fitting fraction of time spent to three pore model for unsmoothed, 7000-point simulations. Positive simulations are generated by

a mock three pore system; negative simulations are generated with randomized parameters for eight states unconstrained by three pore relations. Reprinted with permission from *Drahushuk, L.W. et al. ACS Nano 10, 786-95 (2015)*. Copyright 2015 American Chemical Society.<sup>66</sup>

The coefficient of determination,  $R^2$ , from both the least squares fitting of the states permeance levels,  $SSE_{\Pi}$ , and the fitting of fraction of time spent in each state,  $SSE_P$ , and the resulting fitted values for the individual pores are summarized in Table 8. As shown in Figure 11a, He did not exhibit significant state switching behavior and its fit is included only for comparison. The assignment of fitted values to pores a, b, or c was done according to increasing  $y$  values, the difference between the permeance of high and low states, assuming the trend is consistent between the gases. The exact values of  $x$  and the three  $y_i$  should not be the same for both gases, or even necessarily scale proportionally, as the interaction between the pore and the gas molecule is not simple. However, the three values of  $p_i$ , the likelihoods of the individual pores being in a high or low state, are likely to be properties of the pores themselves; and the fact that the three  $p_i$  values are similar between the three different gases is consistent with this interpretation. A more specific interpretation for the meaning of the  $p_i$  values is given in the below section.

**Table 8.** Summary of three pore model fitting for experimental results for the experimentally measured gases with sample 1.  $N$  is the number of data points;  $R^2$  is the coefficient of determination calculated with the appropriate sum of squared error;  $SSE_{\Pi}$  is defined by; equation (4.16);  $SSE_p$  is defined by equation (4.17); the three  $p_i$  are defined by equation (4.2);  $x$  and the three  $y_i$  are used and defined by equations (4.1).

Gas	N	$R^2(SSE_{\Pi})$	$R^2(SSE_p)$	$p_a$	$p_b$	$p_c$	$x$	$y_a$	$y_b$	$y_c$
							$10^{-23} \text{ mol/(s Pa)}$			
Ne	699	0.97	0.99	0.38	0.37	0.11	0.11	0.08	0.18	0.40
H <sub>2</sub>	484	0.97	0.99	0.46	0.28	0.11	0.32	0.32	0.71	1.47
CO <sub>2</sub>	288	0.95	0.96	0.50	0.21	0.04	0.28	0.49	0.89	2.23
He	109	0.97	0.50	0.36	0.32	0.72	1.36	0.15	0.25	0.32

### 4.3.3 Mechanism for switching

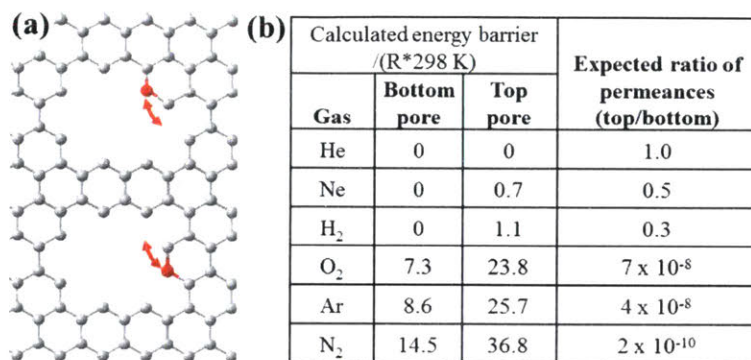
The transport through the pore is limited by the energy barrier the molecule experiences when passing through the pore, as the separation factors between gases exceed the molecular weight based Knudsen selectivities from an effusion mechanism.<sup>45</sup> This barrier energy is different for each molecule-pore combination, and the differences in the barrier energy between molecules are the source of the observed high selectivities. We explain the observed permeance switching as the result of a small rearrangement in the pore, in essence a small chemical change, that alters the energy barrier that the gas molecules experience passing through the pore. Because of the strong dependence on the energy barrier, relatively small changes in the pore can effect a large change in permeance. The large stochastic changes in permeance observed are a direct effect of these molecular scale rearrangements at the pore.

With this view of the switching, we can define clearer meaning to the  $p_i$  values used in the model of the previous section. The  $p_i$  values define the fraction of time the pore spends in each state, and they effectively represent the thermodynamic chemical

equilibrium between the two pore configurations, ultimately a function of the relative free energies of the two configurations. The differences between  $p_a$ ,  $p_b$ , and  $p_c$ , the values for the three pores, in Table 8, stem from differences in the configurations and energies of the three individual pores. The fact that variance for a specific  $p_i$  value across the studied gases with observed fluctuations is much smaller compared to the variance across pores is consistent with this interpretation of stochastic changes in pore configuration.

Additionally, in Figure 11a, the large jumps in permeance are not observed for He. We explain this as a result of the fact that He is the smallest gas tested, significantly smaller than the pore compared to the other gases, and it thus experiences a very small or no barrier to transport through the pore. Because the molecule is significantly smaller than the pore, the slight rearrangement in the pore edges does not significantly affect the barrier energy and therefore does not result in a large permeance change. For the other gases, whose sizes are more commensurate with the pore, the small changes in pore size and chemistry are more impactful. Figure 18 uses Lennard-Jones potentials<sup>69, 70</sup> to calculate the energy barriers for two configurations of a toy pore and demonstrates that He is insensitive to the small change between the two configurations, whereas the predicted permeance change is comparable to the experimentally observed permeance fluctuations for the other gases tested.





**Figure 18.** (a) Example of a small scale rearrangement for a simplified model pore formed from eight carbon atom vacancies. (b) Estimations for energy barrier for gas transport and the associated ratios of expected permeances for He, Ne, H<sub>2</sub>, O<sub>2</sub>, Ar, and N<sub>2</sub> gases. Reprinted with permission from *Drahushuk, L.W. et al. ACS Nano 10, 786-95 (2015)*. Copyright 2015 American Chemical Society.<sup>66</sup>

The frequency at which the switching between permeance states occur can be used to gain a rough estimate of the activation energy for the pore rearrangement. Counting the number of transitions from the Hidden Markov fits for H<sub>2</sub>, Ne, and CO<sub>2</sub>, while excluding any transitions that occur where separate experimental runs are merged together, transitions in permeance states occurred every 15 minutes on average. Considering that three pores are responsible for the transitions, we use an average frequency for the forward transition of 45 minutes. By assuming an Arrhenius dependence with an attempt frequency of 10<sup>13</sup> 1/s, corresponding to the order of magnitude for molecular vibrations,<sup>64</sup> we calculate an activation energy for switching to be 1.0 eV. This value is commensurate with the activation energies for bond rearrangements, such as cis-trans isomerization,<sup>71</sup> which is consistent with the proposed mechanism of small scale rearrangements giving rise to the observed switching in permeance.

## 4.4 Conclusions

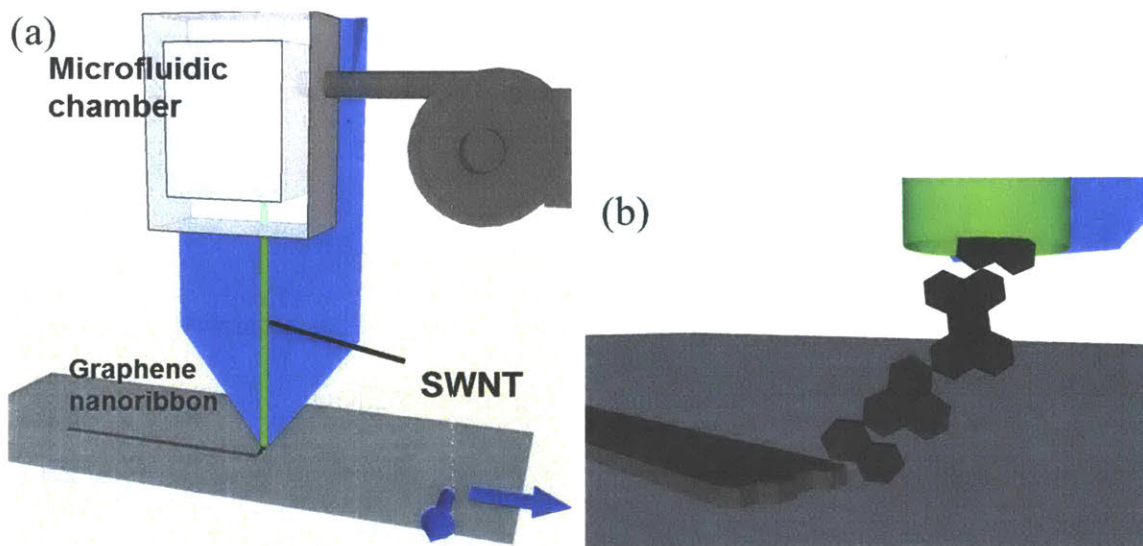
Through analysis based on a three pore Markov network, we showed that the multiple observed states arose from a combination of three independent pores alternating between two states; comparing to simulated data sets to show the quality of the experimental data's fit was within expectations, 15<sup>th</sup> percentile, for a three pore Markov network and outside the range of that for a non-three pore controls, 1<sup>st</sup> percentile. We attributed the source of the fluctuating states for the individual pores to small scale rearrangement in the pore structure, and could estimate the activation energy for switching as 1.0 eV, comparable to the energy required for a bond rearrangement. This chapter highlights the value in the study and consideration of pore stability in theoretical work on graphene membranes, and emphasizes that pore stability and averaging across configurations may play an important role in determining the performance of large scale membranes.

## 5 EXPLORATION OF DIRECT WRITE SYNTHESIS VIA A NANONOZZLE: FUNDAMENTAL SCALING LAWS

### 5.1 Significance of direct write nanoribbon synthesis

The synthesis and placement of nanomaterials at the nano- or atomic scale precision remains a longstanding, largely unsolved challenge of nanotechnology. I explore, at a conceptual level, the viability of using a nanopore as a “nano-nozzle” to localize reagent as a direct write method for synthesis and patterning.

In particular, I will focus on the example case of graphene nanoribbon growth on a substrate. There is significant interest in developing electronic components from graphene nanoribbons, which are predicted<sup>72</sup> and shown<sup>54, 73</sup> to have a favorable bandgap for digital electronic applications, unlike full two dimensional graphene. However, to achieve such a bandgap and maintain the innate high electron mobility of graphene, the nanoribbon must have defect free edges and a width on the order of a nanometer. This has proven difficult to achieve with current fabrication and placement methods in a scalable fashion.<sup>74</sup> A nanonozzle has the ability to localize a small flux of molecules; using this aspect to localize a reagent for nanoribbon growth would yield different results than a bulk reaction. I will seek to evaluate this method and determine the conditions necessary for nanoribbon growth technique, with particular focus on evaluating the predicted width of the nanoribbon. A concept illustration of a device to realize this idea is given in Figure 19.

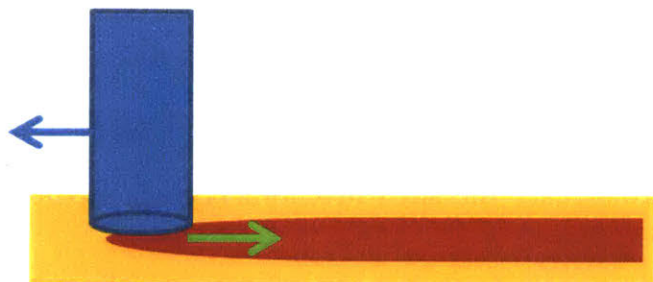


**Figure 19:** (a) Idealized illustration of concept for graphene nanoribbon growth by a nanonozzle formed from a single walled carbon nanotube (SWNT) that delivers reagent to the site of the growing nanoribbon.

## 5.2 Simplified analytical models for describing ribbon growth from a nanonozzle

Graphene growth on a copper surface occurs by first nucleating a seed and then growing outward from the edges in a monolayer. In the following analysis, I will assume a starting seed exists and that a ribbon grows in a monolayer extending from the seed. By localizing the addition of reagent to the region of the ribbon seed, I will assume that the only reaction that occurs is addition to the edges of ribbon and that nucleation of addition seeds is negligible. I will consider a number of models with a range of dimensions and assumptions.

### 5.2.1 1D toy model with diffusion, convection, and reaction



**Figure 20:** (a) Illustration representing 1D model for nanonozzle growth of a nanoribbon; blue arrow represents nozzle movement; green arrow represents diffusion of reagent in the 1D direction; red bar represents growing nanoribbon.

At its simplest, the system can be represented by a quasi-1D model, illustrated in Figure 20, where all material leaving the system through a homogeneous reaction term is added to the width. Width is treated as a variable along the one-dimensional length, but isn't considered in terms of changing the 1D nature of the ribbon. I consider the reference frame to be the tip of the nozzle, such that the movement of the nozzle can instead be written as a constant convective velocity in the x-direction,  $v$ . For simplicity, reagent is only allowed to diffuse in only one direction away from the nozzle. The 1D convection-diffusion equation in this case is as follows in equation (5.1).

$$v \frac{dC}{dx} = D \frac{d^2C}{dx^2} - k_w C \quad (5.1)$$

Where  $C$  is the 1D concentration,  $D$  is the diffusion coefficient, and  $k_w$  is the rate constant for a first order reaction representing the growth in width of the nanoribbon. The solution to this equation is given by equation (5.2), where  $C_i$  is the concentration at  $x=0$ .

$$C(x) = C_i e^{\frac{v - \sqrt{4Dk_w + v^2}}{2D}x} \quad (5.2)$$

Note that  $C_i$  can alternatively be replaced with a term derived from a constant flow of material from the nanonozzle outlet,  $n$ . This alternative form is given by equation (5.3).

$$C(x) = \frac{n}{\sqrt{k_w(D - n/2\sigma)}} e^{\frac{v - \sqrt{4Dk_w + v^2}}{2D}x} \quad (5.3)$$

The growth rate of the width at any given point  $x$  can then be described by equation (5.4), where  $\sigma$  is the areal density of graphene.

$$\frac{dW(x)}{dt} = k_w C(x) \frac{1}{\sigma} \quad (5.4)$$

To follow a fixed point along the ribbon in time, I account for the moving reference frame by making the substitution  $x \rightarrow vt$ . The expression can then be integrated over time to find the final nanoribbon width, as setup in equation (5.5) and solved in equation (5.6), with  $W_0$  representing the minimum width defined by the leading edge of the nanoribbon.

$$W|_{t \rightarrow \infty} = W_0 + \int_0^{\infty} \frac{k_w}{\sigma} C(x = vt) dt \quad (5.5)$$

$$W|_{t \rightarrow \infty} = W_0 + \frac{C_i}{2\sigma} \left( 1 + \sqrt{\frac{4Dk_w}{v^2} + 1} \right) \quad (5.6)$$

Equation (5.6) provides a measure of the effect of diffusion on the width of the nanoribbons. In this simple 1D model, all material ends up as part of the nanoribbon, therefore there is a minimum width ( $W_0 + C_i / \sigma$ ) in the limit of no diffusion. However, diffusion can result in a larger width according to the size of the term  $(4 D k_w v^{-2})$ . Considering that the maximum translation speed of the nanoribbon is the growth rate along the length of the tube, as described by  $v = k_l C_i / \sigma$ , then this term can be rewritten as follows.

$$W|_{t \rightarrow \infty} = W_0 + \frac{C_i}{2\sigma} \left( 1 + \sqrt{\frac{4 D k_w \sigma^2}{(k_l C_i)^2} + 1} \right) \quad (5.7)$$

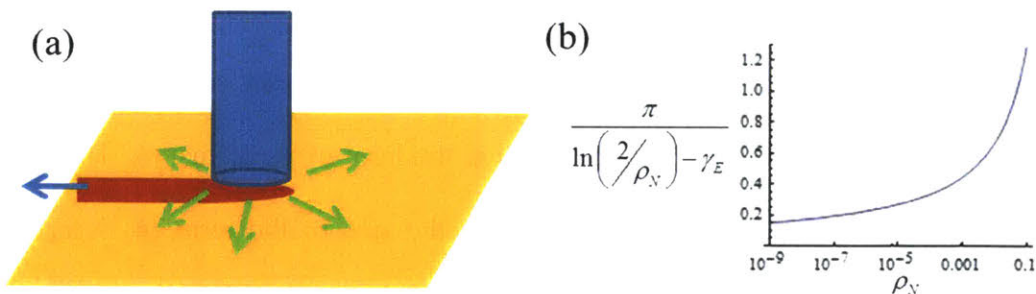
And further simplification assuming  $k = k_l = 0.5 k_w$ , that the growth rate at for both the width and the length is the same (accounting for the fact two edges are associated with growth of the width), equation (5.7) can be further simplified in the limit of low concentration, as shown in equation (5.8);

$$W|_{\substack{t \rightarrow \infty \\ C_i \rightarrow 0}} = W_0 + \sqrt{\frac{2D}{k}} \quad (5.8)$$

This form highlights that the ratio of diffusion to reaction is what controls the minimum achievable width, which will be consistent with the next model as well.

### 5.2.2 2D model with diffusion and reaction





**Figure 21:** (a) Illustration representing 2D model for nanonozzle growth of a nanoribbon; blue arrow represents stage movement; green arrows represent diffusion of reagent in the 2D plane of the substrate; red bar represents growing nanoribbon. (b) Semi-log plot of component in equation (5.17) for nanoribbon width that is determined by the non-dimensionalized nanonozzle size,  $\rho_N$ .

Though simple, the 1D is further removed from a physical system. A 2D model, illustrated in Figure 21a, adds back some of the complexity. In a 2D perspective, reagent leaves the nanonozzle and spreads out via diffusion in a plane, with the motion of the nozzle relative to the substrate acting as an effective convection term. This full 2D case becomes too complex for an analytical solution; however, considering the case where convection is negligible and adding a first order consumption term across the entire surface, not only at the ribbon edge, yields usable results.

Ignoring convective terms appears to be a reasonable simplification under the assumption that the growth rate will be similar to the rates of current CVD growth processes for graphene, which advance at a rate of order  $1 \mu\text{m}/\text{min}$ .<sup>74, 75</sup> Comparing this to diffusion coefficients in air, which are of order  $10^{-6}$ , reveals that the Peclet number, the ratio of convective to diffusive contributions, is negligible at length scales smaller than  $\sim 10 \text{ m}$ , and can therefore be ignored as I am considering length scales on the order of nanometers. The inclusion of a first order consumption term is not as readily justified.



From the perspective of diffusion on a surface, it can be considered the rate at which reagent desorbs from the surface and is lost. It can also be considered a proxy term to represent mass transport from the nanoribbon. By including without rigorously justifying those perspectives, I will only use the results drawn from this model as qualitative observations that will inform the direction for more advanced models.

These assumptions allow the differential equation to be simplified in radial coordinates in equation (5.9), where  $k_{-A}$  is the rate constant of the first order consumption term.

$$\frac{D}{r} \frac{\partial}{\partial r} \left( r \frac{\partial C}{\partial r} \right) - k_{-A} C = 0 \quad (5.9)$$

The solution is described by equation (5.10), with A as a constant to be defined by the boundary condition,  $K_0$  being the modified Bessel function of the 2<sup>nd</sup> kind, and  $\rho$  as non-dimensionalized radius.

$$C(r) = A K_0 \left( \frac{r}{\sqrt{D/k_{-A}}} \right) = A K_0(\rho) \quad (5.10)$$

The boundary condition is defined in equation (5.11) as a constant flux outwards at the dimensionless nanonozzle radius,  $\rho_N$ .

$$\text{BC: } n = -2\pi \rho_N D \left. \frac{dC}{d\rho} \right|_{\rho_N} \quad (5.11)$$

As done previously, tracking the width at a given point on the substrate can be related to an integral along the length, as defined in equation (5.12).

$$W = W_0 + \int_{\rho_N}^{\infty} \frac{k_w}{v\sigma} A K_0(\rho) \sqrt{D/k_{-A}} d\rho \quad (5.12)$$

In this case, there is not a general analytical solution with a simple form. However, making the assumption that  $\rho_N$ , the nanonozzle radius, is small, the simplifications described by equations (5.13) to (5.17) are possible.

$$\lim_{\rho_N \rightarrow 0} \int_{\rho_N}^{\infty} K_0(\rho) d\rho = \pi/2 \quad (5.13)$$

$$\lim_{\rho_N \rightarrow 0} A = \frac{n}{2\pi D} \quad (5.14)$$

$$\lim_{\rho_N \rightarrow 0} C(\rho_N) \sim \frac{n}{2\pi D} \left( \ln\left(\frac{2}{\rho_N}\right) - \gamma_E \right) + O(\rho^2) \quad (5.15)$$

$$\lim_{\rho_N \rightarrow 0} W = W_0 + \frac{nk_w\omega}{4v\sqrt{Dk_{-A}}} = W_0 + \frac{n}{2C(\rho_N)\sqrt{Dk_{-A}}} \quad (5.16)$$

$$\lim_{\rho_N \rightarrow 0} W = W_0 + \sqrt{\frac{D}{k_{-A}}} \frac{\pi}{\ln\left(\frac{2}{\rho_N}\right) - \gamma_E} \quad (5.17)$$

$\gamma_E$  is Euler's constant. The combined value of the numeric terms in equation (5.17) is plotted in Figure 21b. An important observation from the result of this limit is that the flow out of the nozzle cancels out of the final expression for width. This removes

an intuitive parameter to control growth, and emphasizes the importance of the length scale defined by the ratio of diffusion to reaction rate. In practice, the width can always be made larger by operating a lower velocity than the maximum possible, but the minimum width is strictly defined by the transport and chemical properties.

### **5.3 Models and Simulations in 3D**

The various lower dimensional models highlighted the importance of the consumption term in obtaining a finite width and determining the minimum width possible nanoribbons grown from a nanonozzle. However, in the models this term was poorly defined as a quasi-homogenous reaction, despite the fact that it can only occur at the ribbon edges. To evaluate the feasibility of a nanonozzle system for nanoribbon growth, I performed simulations that more accurately represent the reaction occurring only at the edges of the nanoribbon. In the simple 2D model, the consumption term did not have a rigorous physical definition; it is important to determine whether or not reaction only at the edges is sufficient to yield a finite width nanoribbon, as well as provide a measure to evaluate the basic correlations implied by the simple models.

### 5.3.1 Nanonozzle Simulations

**Table 9:** Summary of relevant parameters in the nanonozzle system in three dimensions.

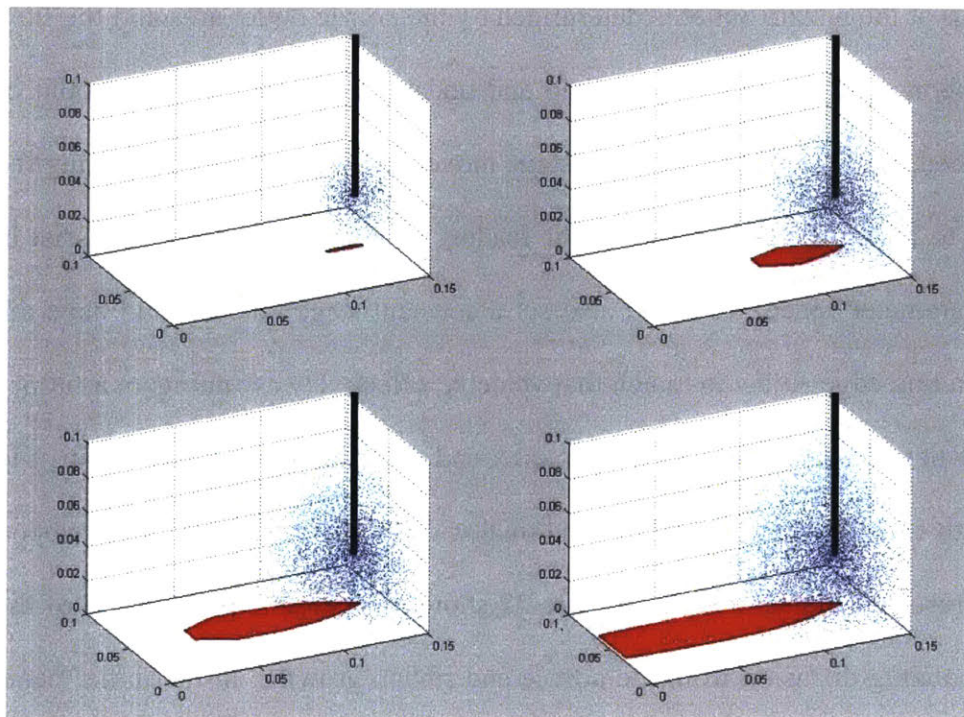
	<b>Description</b>	<b>SI units</b>
D	Diffusion constant	$\text{m}^2 \text{s}^{-1}$
k	Edge reaction constant	$\text{m}^2 \text{s}^{-1}$
$\sigma$	Material area per mass	$\text{m}^2 \text{mol}^{-1}$
h	Nozzle outlet height	m
Q	Reagent flow rate out of nozzle	$\text{mol s}^{-1}$
v	Stage translation velocity	$\text{m s}^{-1}$
r	Nozzle outlet radius	m
X	Distance from nozzle outlet along surface	m
W	Ribbon width at distance X	m

To explore this concept, we developed a simple simulation of the system. The definitions of the relevant parameters are summarized in Table 9. We assume that the growth occurs as a monolayer ribbon, growing only at the edges of the existing ribbon, and starting from a seed at the beginning of the simulation. Considering the case of transport by diffusion only, we applied the following equations for the simulation, with  $C$  as the concentration of reagent.

$$\frac{dC}{dt} = D \left( \frac{d^2C}{dx^2} + \frac{d^2C}{dy^2} + \frac{d^2C}{dz^2} \right) + gen \quad (5.18)$$

$$gen = \begin{cases} const & @ \text{ nozzle outlet} \\ -kC & @ \text{ ribbon edge} \\ 0 & else \end{cases} \quad (5.19)$$

The *const* at the nozzle outlet is determined by the nozzle outlet area and the flow rate,  $Q$ . The ribbon edge position was tracked and updated according to the amount of material consumed from the gas phase. The stage movement was applied by shifting the ribbon position to match the growth rate at the leading edge of the ribbon. To assist in exploring the parameter space, we could also set a constant stage velocity and have the growth at the leading edge adjust to match that velocity, effectively assuming an arbitrary anisotropic growth rate that allows the ribbon to extend at the appropriate rate relative to the defined width extension rate constant. The final width along the length of the ribbon is saved as the result of the simulation. Figure 22 shows an example progression of the simulation, visualizing diffusion from the nozzle and ribbon growth. In the initial pane, the stage has not begun moving, as the reagent has not yet diffused to the enough to reach the ribbon seed below. In subsequent panes, the stage is moving to match the growth rate of the leading edge of the ribbon, resulting in an elongated island and eventual ribbon.



**Figure 22:** Example progression of diffusion from nanonozzle and nanoribbon growth. Red illustrates the monolayer coverage of the ribbon; black cylinder represents nozzle delivering reagent above the surface; dot density and color vary as a visualization of a continuous 3D, gas phase reagent concentration profile.

### 5.3.2 Low Reaction Rate 3D Analytical Solution

The previous lower dimensional models were simple enough to be solved with including a reaction term, giving insight into the importance of the ratio of reaction and diffusion. However, to compare to the simulations directly, we will need to use a three dimensional model. In order to solve for this case, we will have to assume the reaction is negligible relative to diffusion, meaning the growth of the ribbon does not influence the concentration profile in the gaseous phase. A first order reaction rate will still control the rate at which width increases.

With that assumption, we start with the solution for diffusion from a point source above a surface, given by equation (5.20) below. This provides an approximate solution for the case of low reaction rate at the surface.

$$C(r, z) = \frac{Q}{4\pi Dh} \left( \frac{1}{\sqrt{\left(\frac{z}{h}-1\right)^2 + \left(\frac{r}{h}\right)^2}} + \frac{1}{\sqrt{\left(\frac{z}{h}+1\right)^2 + \left(\frac{r}{h}\right)^2}} \right) \quad (5.20)$$

where  $Q$  is the molar flow rate from the nozzle,  $D$  is the diffusion constant, and  $h$  is the height of the nozzle outlet above the growth surface. Considering only the concentration at the surface, the equation becomes:

$$C(z = 0) = \frac{Q}{2\pi D} \frac{1}{\sqrt{h^2 + r^2}} \quad (5.21)$$

If we make the assumption that the consumption of material due to reaction is small relative to the rate at which material is supplied via diffusion, then this equation can be used to calculate the width a nanoribbon. For a first order reaction, the growth rate of the ribbon width,  $W$ , can be defined in terms of the concentration profile.

$$\frac{dW}{dt} = 2k_w \sigma C \quad (5.22)$$

$k_w$  is the reaction rate constant for growth from a ribbon edge in the width direction, and  $\sigma$  is the molar surface area. Assuming the ribbon width is small relative to the length scale of the system, the radial position,  $r$ , at the ribbon edge can be simplified to the rectangular coordinate  $x$ . Considering the  $v$  as a constant velocity for stage

translocation to be equal to the rate of change in surface position,  $dx/dt$ , the ribbon growth rate can be integrated along length,  $x$ , to find the ribbon width at a fixed distance from the nozzle.

$$\int_0^{W_1} dW = \frac{k_w \sigma Q}{\pi D v} \int_0^{X_1} \frac{1}{\sqrt{h^2 + x^2}} dx \quad (5.23)$$

$$W_1 = \frac{k_w \sigma Q}{\pi D v} \operatorname{arcsinh} \left( \frac{X_1}{h} \right) \quad (5.24)$$

In order to grow a continuous ribbon, the velocity at which the stage translates below the nozzle must not exceed the rate of at which the ribbon can grow in length from its leading edge. This constraint gives a definition for maximum velocity in terms of the  $k_l$ , the rate constant for growth from an edge in the length direction, which is equal to  $k_w$  in the case of anisotropic surface growth, and the maximum reagent concentration occurring under the nozzle.

$$v_{\max} = k_l \sigma C(r = 0, z = 0) \quad (5.25)$$

$$v_{\max} = \frac{k_l \sigma Q}{2\pi D h} \quad (5.26)$$

Operating at the maximum velocity results in the minimum ribbon width, so this operating state is of particular interest. Applying the definition of  $v_{\max}$  in equation (5.26) to the solution for ribbon width in equation (5.24) yields the following.

$$W_{1, v \rightarrow v_{\max}} = 2h \operatorname{arcsinh} \left( \frac{X_1}{h} \right) \quad (5.27)$$



The minimum ribbon width in equation (5.27) at a fixed distance becomes dependent only on the length scale in the system, the nozzle outlet height,  $h$ . It also does not converge to a finite width. To apply this concept practically to a real system, additional phenomenon in the system will need to be considered to achieve finite width that is below the minimum described by equation (5.27). One relevant approach is to apply local heating to define a more limited reaction zone. Another is to apply a convective flow to the system, which would allow the concentration, and therefore reaction rate as well, to drop off faster than diffusion alone.

### 5.3.3 Non-dimensional Notation

Buckingham Pi analysis can reduce the number of relevant variables to a smaller set of dimensionless variables. Table 9 summarizes all the relevant variables in the system. Applying the analysis to this system and choosing some recognizable dimensionless groups yields the following equations.

$$\Pi_1 = \frac{k}{D} \quad (5.28)$$

$$\Pi_2 = \frac{h}{r} \quad (5.29)$$

$$\Pi_3 = \frac{D}{h\nu} \quad (5.30)$$

$$\Pi_4 = \frac{\sigma Q}{k} \quad (5.31)$$

$$\Pi_5 = \frac{X}{r} \quad (5.32)$$

$$\Pi_6 = \frac{W}{r} \quad (5.33)$$

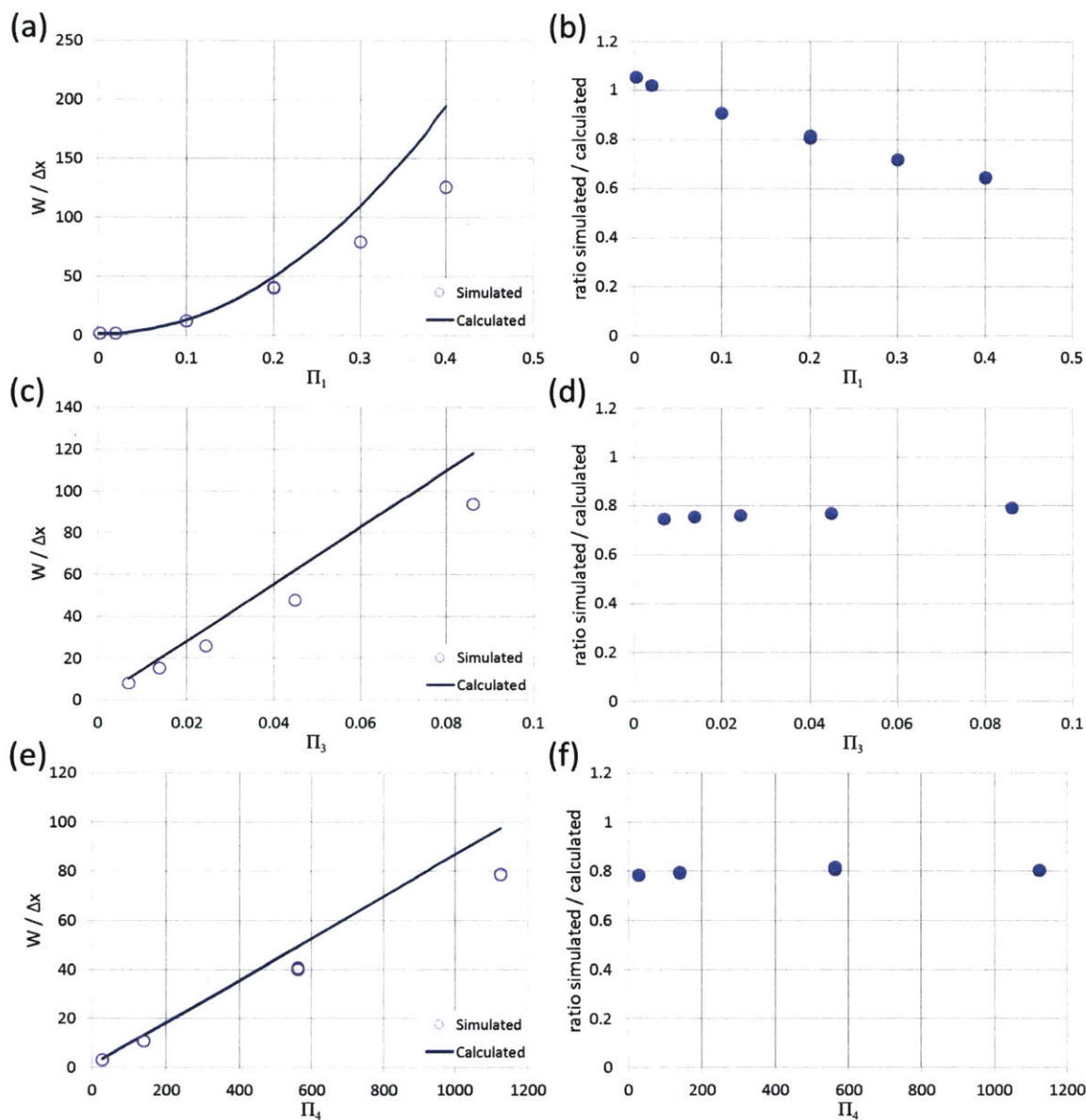
$\Pi_1$  is the Damköhler number in the system;  $\Pi_2$  is the height length scale ratio;  $\Pi_3$  is a quasi-Peclet number as the ratio diffusion to stage movement; and  $\Pi_4$  is a ratio of mass between the gas phase and the surface;  $\Pi_5$  is the length scale ratio for distance along the ribbon; and  $\Pi_6$  is the length scale ratio for the width of the ribbon. The previously derived analytical expressions can be rewritten in terms of these  $\Pi_i$ . The analytical solution for ribbon width, equation (5.24), rewritten in terms of  $\Pi_i$  is:

$$\Pi_6 = \frac{\Pi_1^2 \Pi_2 \Pi_3 \Pi_4}{\pi} \operatorname{arcsinh} \left( \frac{\Pi_5}{\Pi_2} \right) \quad (5.34)$$

Additionally, the definition of maximum velocity for low reaction rates given by equation (5.26), which is a requirement of continuous growth, can be rewritten in term of  $\Pi_i$  as well as a growth extension inequality.

$$1 < \frac{\Pi_1^2 \Pi_3 \Pi_4}{2\pi} \quad (5.35)$$

## 5.3.4 Comparison between 3D Model and Simulations

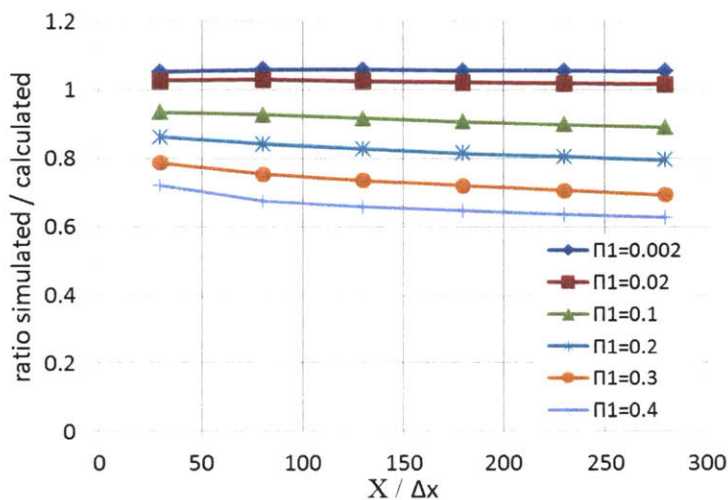


**Figure 23:** A comparison between the simulated results for ribbon width when varying (a)  $\Pi_1 = k/D$ , (c)  $\Pi_3 = D/(h v)$ , and (e)  $\Pi_4 = \sigma Q/k$  compared to the calculated analytical solution from equation (5.24), which is derived in the limit of low reaction rate. The ratio of simulated to calculated ribbon width is also given for (b)  $\Pi_1$ , (d)  $\Pi_3$ , and (f)  $\Pi_4$ . The full parameters and corresponding Pi group values of the simulations discussed above are summarized in Table 10 to Table 13.

Figure 23 plots the steady state ribbon width at a fixed distance along the ribbon for a range of different parameter, comparing the results to the analytical solution in equation (5.24). The primary approximations that were made to justify the derivation of the analytical solution were that the reaction for ribbon growth does not alter the concentration profile from the no reaction case, that diffusion occurs from a point source, and that the ribbon width is small relative to the length scale. The first assumption, that the concentration profile is unperturbed by the reaction, is represented by the Damköhler number,  $\Pi_1 = k/D$ . When  $\Pi_1$  is low the reaction rate, the rate at which material is depleted from the gaseous phase to form the growing ribbon, is low relative to the rate at which diffusion transports material, and the concentration profile is undisturbed. This can be seen in Figure 23b, where the ratio of the simulated ribbon width to that calculated width diverges from 1 at higher  $\Pi_1$  values. Figure 23d demonstrates the contrast when  $\Pi_3$  varies, as the ratio is nearly independent of  $\Pi_3$ , holding steady around the value expected the constant value of  $\Pi_1 = 0.2$  used in all runs in Figure 23d. The same holds true for  $\Pi_4$ , shown in Figure 23f, not being a factor in the degree the simulations diverge from the analytical calculations.

The approximation of the analytical solution that diffusion occurs from a point source is held simply with the condition that is  $\Pi_2 = h/r$  is large; if height of the nozzle outlet above the surface is large relative to the radius of the nozzle outlet, then the outlet can be approximated as a point source. The simulations used values of  $\Pi_2 = 20$ . The final approximation, that the width is small relative to the length scale of the system is more difficult to define distinctly. In the case of an approximate point source, the most appropriate expression is that  $\Pi_6/\Pi_2 = W/h$  should be small when  $X \sim h$ . This value,  $W/h$

when  $X=h$ , ranges from 0.0001 to 2 in the above simulated results depicted in Figure 23c and d, so it may contribute to the divergence of the simulated results from the calculated for some of the points.



**Figure 24:** A comparison between the simulated results for ribbon width and the calculated analytical solution from equation (5.24) when along the length of the simulated ribbon for a range of  $\Pi_1 = k/D$ , values.

The widths reported in Figure 23 occurred at a constant lateral distance,  $X / \Delta x = 180$ , from the nozzle. Figure 24 illustrates the ratio of the simulated width to the analytically calculated along the full length of the simulation for the various  $\Pi_1$  values shown in Figure 23b. As shown, the divergence of the simulated results from the calculated does vary slightly along the length of the ribbon, though not as strongly as the variation with  $\Pi_1$ .

The full parameters and corresponding Pi group values of the simulations discussed above are summarized in Table 10 to Table 13.  $\Pi_1$ ,  $\Pi_2$ ,  $\Pi_3$ , and  $\Pi_4$  are defined by equations (5.28)-(5.31). Box length, width, and height refer to the size of the

simulation.  $\Delta x$ ,  $\Delta y$ ,  $\Delta z$  refer to voxel size in the respective length, width, and height dimensions.  $\Delta t$  is the time step size. Nozzle outlet x-, y-, and z-positions refer to the location position of the center of nozzle outlet; nozzle size sets the length of a side of a square nozzle outlet, which sets the positions in the  $xy$  plane that are treated as the nozzle outlet defined by equation (5.19).  $Q$ ,  $D$ ,  $\sigma$ ,  $v$ , and  $k$  are defined in Table 9.

**Table 10.** Pi group values and varying simulation parameters for results in Figure 23a-b.

run #	1	2	3	4	5	6	7	8	9	10
$\Pi_1$	0.002	0.02	0.1	0.2	0.2	0.2	0.2	0.2	0.3	0.4
$\Pi_2$	0.019	0.019	0.019	0.019	0.019	0.019	0.019	0.019	0.019	0.019
$\Pi_3$	0.086	0.086	0.086	0.086	0.086	0.086	0.086	0.086	0.086	0.086
$\Pi_4$	563	563	563	563	563	563	563	563	563	563
$Q$	5.63E-11	5.63E-11	5.63E-11	5.63E-11	1.13E-10	5.63E-11	5.63E-11	5.63E-11	5.63E-11	5.63E-11
box length / $\Delta x$	400	400	400	200	200	400	400	800	400	400
box width / $\Delta y$	160	160	160	100	100	160	240	240	160	160
box height / $\Delta z$	70	70	70	60	60	70	90	90	70	70
$D$	0.001	0.001	0.001	0.001	0.001	0.001	0.001	0.001	0.001	0.001
$\sigma$	2.0E+07	2.0E+08	1.0E+09	2.0E+09	1.0E+09	2.0E+09	2.0E+09	2.0E+09	3.0E+09	4.0E+09
$v / (\Delta x / \Delta t)$	0.4	0.4	0.4	0.4	0.4	0.4	0.4	0.4	0.4	0.4
$k$	2.0E-06	2.0E-05	1.0E-04	2.0E-04	2.0E-04	2.0E-04	2.0E-04	2.0E-04	3.0E-04	4.0E-04

**Table 11.** Pi group values and varying simulation parameters for results in Figure 23c-d.

run #	11	12	13	14	15
$\Pi_1$	0.2	0.2	0.2	0.2	0.2
$\Pi_2$	0.019	0.019	0.019	0.019	0.019
$\Pi_3$	0.005	0.011	0.022	0.043	0.086
$\Pi_4$	1125	1125	1125	1125	1125
Q	1.13E-10	1.13E-10	1.13E-10	1.13E-10	1.13E-10
box length / $\Delta x$	400	400	400	400	400
box width / $\Delta y$	240	240	240	240	240
box height / $\Delta z$	90	90	90	90	90
D	0.001	0.001	0.001	0.001	0.001
$\sigma$	2.0E+09	2.0E+09	2.0E+09	2.0E+09	2.0E+09
$v / (\Delta x/\Delta t)$	6.4	3.2	1.6	0.8	0.4
k	2.0E-04	2.0E-04	2.0E-04	2.0E-04	2.0E-04

**Table 12.** Pi group values and varying simulation parameters for results in Figure 23e-f.

run #	16	17	18	19	20	21	22	23	24	25
$\Pi_1$	0.2	0.2	0.2	0.2	0.2	0.2	0.2	0.2	0.2	0.2
$\Pi_2$	0.019	0.019	0.019	0.019	0.019	0.019	0.019	0.019	0.019	0.019
$\Pi_3$	0.086	0.086	0.086	0.086	0.086	0.086	0.086	0.086	0.086	0.086
$\Pi_4$	28	141	141	563	563	563	563	563	563	1125
Q	5.63E-11	1.41E-11	5.63E-11	5.63E-11	1.13E-10	5.63E-11	5.63E-11	5.63E-11	5.63E-11	5.63E-11
box length / $\Delta x$	400	200	200	200	200	400	400	800	400	400
box width / $\Delta y$	240	100	100	100	100	160	240	240	240	240
box height / $\Delta z$	90	60	60	60	60	70	90	90	90	90
D	0.001	0.001	0.001	0.001	0.001	0.001	0.001	0.001	0.001	0.001
$\sigma$	1.0E+08	2.0E+09	5.0E+08	2.0E+09	1.0E+09	2.0E+09	2.0E+09	2.0E+09	2.0E+09	4.0E+09
$v / (\Delta x/\Delta t)$	0.4	0.4	0.4	0.4	0.4	0.4	0.4	0.4	0.4	0.4
k	2.0E-04	2.0E-04	2.0E-04	2.0E-04	2.0E-04	2.0E-04	2.0E-04	2.0E-04	2.0E-04	2.0E-04

**Table 13.** Simulation parameters that are held constant for all results in Figure 23.

$\Delta x$	0.001
$\Delta y$	0.001
$\Delta z$	0.001
$\Delta t$	0.0001
nozzle size / $\Delta x$	3
(nozzle outlet x-position) / $\Delta x$	20
(nozzle outlet y-position) / (box width)	0.5
(nozzle outlet z-position) / $\Delta z$	30

### 5.3.5 Towards Realizing an Experimental Nanonozzle System

Perfecting an experimental nanonozzle system for nanoribbon synthesis and patterning will be a significant experimental endeavor. However, there are established elements which can provide a starting point; tips for near-field scanning optical microscopy (NSOM) normally provide a conduit for light to pass through an aperture ranging from tens to hundreds of nanometers in diameter, and operate at a distance of tens of nanometers above a surface.<sup>76</sup> Interfacing an NSOM tip with a nanofluidic conduit instead of light is an approach that can take advantage of existing technology for controlling a tip at a short distance from a surface.

Table 14 takes geometric estimates from an NSOM tip along with physical parameters based on graphene and current graphene synthesis to summarize values for the relevant parameters to an experimentally realizable nanonozzle system.



**Table 14:** Estimates for values for relevant parameters to experimentally realizable nanonozzle system.

Variable	Description	SI units	Est. Value	Est. Source
D	Diffusion constant	$\text{m}^2 \text{s}^{-1}$	$10^{-5}$	diffusion of methane in air <sup>77</sup>
k	Edge reaction constant	$\text{m}^2 \text{s}^{-1}$	$9 \times 10^{-6}$	equation (5.26)
$\sigma$	Material area per mass	$\text{m}^2 \text{mol}^{-1}$	$6.1 \times 10^{-5}$	graphene material property
h	Nozzle outlet height	m	$5 \times 10^{-8}$	50nm as achievable height
Q	Reagent flow rate out of nozzle	$\text{mol s}^{-1}$	$10^{-13}$	Hagen–Poiseuille estimate for max nozzle flow w/ water as proxy for reagent
v	Stage translation velocity	$\text{m s}^{-1}$	$1.7 \times 10^{-11}$	target velocity
r	Nozzle outlet radius	m	$5 \times 10^{-8}$	NSOM tip aperture

In

Table 14, an arbitrary reaction is assumed to occur with a reagent of similar diffusivity to the current common graphene feedstock, methane. We assume a minimum stage velocity of 1 nm/min for an experimental result and use equation (5.26) for maximum stage velocity to calculate a necessary edge reaction rate, k, of  $9 \times 10^{-6}$  for such a system. This provides a benchmark for choosing possibly reaction chemistries for an experimental demonstration.

## 5.4 Conclusions and Outlook for Nanonozzle

The preceding work establishes a variety of models for predicting the behavior and relevant parameters of a nanonozzle system for nanoribbon synthesis. The nanonozzle has the potential to be a novel approach to nanoribbon synthesis and patterning, as well as nanopatterning more generally. The 3D analytical model provides a simple and reasonably accurate estimation for the expected ribbon resulting from nanonozzle growth, validated by the more complex nanonozzle simulations. Such simulations would allow exploration of a wider range of conditions in future work on this topic, exploring things like reactions other than first-order, imposed convection, local heating, and other effects that can provide more control over the ribbon width. Simulations can also be used to provide an estimate of the sensitivity in the system to perturbations in the operating conditions, looking at the non-steady states results from perturbations as a measure of quality. The models provide a means for estimating the necessary specifications for eventually experimentally realizing nanoribbon synthesis via a nanonozzle.

## 6 CONCLUSIONS AND FUTURE APPLICATIONS

The focus of my work has been the investigation of transport at the nanoscale, considering how nanomaterials define separations (chapters 2 and 3), how the stochastic behavior of nanopores can change the results of gas transport (chapters 3 and 4), and how the nanopores might be used in conjunction with diffusion as a new method for nanoscale CVD growth (chapter 5).

I began with a fundamental look at the transport through 2D membranes, an emerging field with basic principles distinct from standard, finding similarities to heterogeneous catalysis. This theory established a framework to understand molecular dynamics simulations and experiments, defining contributions from simple gas phase transport with a pore as well as transport via an adsorbed phase. Aspects of both types of transport have been seen in subsequent experiments in the literature. Knudsen selectivities have been demonstrated for small molecules and larger pores,<sup>49, 50, 78, 79</sup> consistent with expectations for nanopores in general; in addition, larger molecules of CO<sub>2</sub> and N<sub>2</sub>O have been observed to greatly exceed the flow rates expected by the Knudsen model relative to He and H<sub>2</sub>,<sup>45</sup> indicative of a significant contribution from an adsorbed phase. These models and the general framework will continue to be useful as more experimental single layer graphene membranes are developed and tested; additional experimental results and simulations will refine the preliminary estimations used in the models.

Applying the understanding of the fundamentals gained from developing the models of gas transport through 2D membranes, in chapter 3, I extracted time-varying gas transport characteristics from experimental data for graphene membranes collected by our collaborators in the Bunch lab. The graphene membrane was suspended over a microcavity and deflected upwards after the microcavity was pressurized. The deflection of the microcavity was monitored with AFM as a means to measure the flow of gas out of the microcavity. As a batch process, the microcavity can be tested as it deflates and then repressurized. A mechanical model of the graphene deflection allowed us to correlate the change in deflection to the flowrate. Additional analysis beyond that allowed us to determine that the flow rate was switching stochastically between different states, both between different runs and within a single run of measuring the deflation. These stochastic changes were attributed in changes to spontaneous changes to the pore configuration, as an activated process with an approximate energy barrier of 1.0 eV, consistent with the energy of molecular rearrangements. The equations applied correspond to the experimental platform used by the Bunch group, with a layer of graphene covering a microcavity, which is useful as a way to investigate permeation over a small area, allowing for a more fundamental probe of graphene pores than large area membranes with many pores. Additionally, the understanding of how to look for and treat stochastic changes is applicable to any platform with few nanopores.

Beyond recognizing and adapting the gas transport analysis for stochastic behavior, in chapter 4, I established three pores as responsible for the different permeance states observed in the experimental data and fit parameters to the individual three pores. In the experimental etching, the membrane is briefly exposed to UV induced oxidative

etching before checking if the deflection has changed; this is repeated until at least one pore forms, at which point the deflection will have dropped significantly due to the higher leak rate of gas out of the microcavity. Due to this method, we expect one or few pores to form, but the exact number is unknown. Because the individual states of the pores could not be observed, Hidden Markov model style analysis was used to fit the states. The results were shown to be consistent with three pores that switch between two states. In addition, to establish confidence, I generated Monte Carlo style simulated data sets of the same size as the experimental data set. Applying the same analysis to these simulated data sets allowed us to establish confidence in the assignment of the limited experimental data set. Stochastic changes are frequently observed in aqueous nanoporous systems,<sup>80</sup> but this is the first time they have been observed in gas phase transport.

In chapter 5, I explored the concept of using a nanonozzle for the model application of direct write growth of graphene nanoribbons, but more generally as a platform for nanoscale patterning and growth. Applying our familiarity with nanopores, the concept is to use a nanopore to locally deliver a precursor for a CVD reaction in such a way that a nanoscale pattern will grow, with diffusion creating a concentration gradient. I used a combination of analytical models and simulation to predict the behavior of such a system, showing the expected and simulated dependence on a selection of nondimensional groups of parameters. The analysis revealed some limitations of the approach in its simplest form in terms of controlling ribbon width and achieving constant growth, motivating further study with additional phenomenon, such as imposed convection or local heating, included. Beyond those additions, future studies could investigate the effects of perturbations and disturbances in the system on the output

ribbon quality to establish the resilience of the platform. Eventually, this line of study can help experimental design and implement of a nanonozzle system. Also, the concepts behind the nanonozzle could be applied more generally to CVD systems as a means of using confinement and localization to achieve novel growth geometry.

## 7 BIBLIOGRAPHY

1. Du, H.; Li, J.; Zhang, J.; Su, G.; Li, X.; Zhao, Y. Separation of Hydrogen and Nitrogen Gases with Porous Graphene Membrane. *The Journal of Physical Chemistry C* 2011, 115, 23261-23266.
2. Geim, A. K. Graphene: status and prospects. *Science (New York, N.Y.)* 2009, 324, 1530-4.
3. Geim, A. K.; Novoselov, K. S. The rise of graphene. *Nature materials* 2007, 6, 183-91.
4. Nair, R. R.; Wu, H. A.; Jayaram, P. N.; Grigorieva, I. V.; Geim, A. K. Unimpeded Permeation of Water Through Helium-Leak-Tight Graphene-Based Membranes. *Science* 2012, 335, 442.
5. Kang, J.; Shin, D.; Bae, S.; Hong, B. H. Graphene transfer: key for applications. *Nanoscale* 2012, 4, 5527-5537.
6. Ni, Z. H.; Wang, H. M.; Kasim, J.; Fan, H. M.; Yu, T.; Wu, Y. H.; Feng, Y. P.; Shen, Z. X. Graphene Thickness Determination Using Reflection and Contrast Spectroscopy. *Nano letters* 2007, 7, 2758-2763.
7. Bunch, J. S.; Verbridge, S. S.; Alden, J. S.; van der Zande, A. M.; Parpia, J. M.; Craighead, H. G.; McEuen, P. L. Impermeable Atomic Membranes from Graphene Sheets. *Nano letters* 2008, 8, 2458-62.
8. Hu, S.; Lozada-Hidalgo, M.; Wang, F. C.; Mishchenko, A.; Schedin, F.; Nair, R. R.; Hill, E. W.; Boukhvalov, D. W.; Katsnelson, M. I.; Dryfe, R. A. W.; Grigorieva, I. V.; Wu, H. A.; Geim, A. K. Proton transport through one-atom-thick crystals. *Nature* 2014, 516, 227-230.

9. Schrier, J. Carbon Dioxide Separation with a Two-Dimensional Polymer Membrane. *ACS applied materials & interfaces* 2012, 4, 3745-3752.
10. Ambrosetti, A.; Silvestrelli, P. L. Gas Separation in Nanoporous Graphene from First Principle Calculations. *Journal of Physical Chemistry C* 2014, 118, 19172-19179.
11. Schrier, J. Helium Separation Using Porous Graphene Membranes. *The Journal of Physical Chemistry Letters* 2010, 1, 2284-2287.
12. Shan, M.; Xue, Q.; Jing, N.; Ling, C.; Zhang, T.; Yan, Z.; Zheng, J. Influence of chemical functionalization on the CO<sub>2</sub>/N<sub>2</sub> separation performance of porous graphene membranes. *Nanoscale* 2012, 4, 5477-82.
13. Liu, H.; Dai, S.; Jiang, D.-e. Insights into CO<sub>2</sub>/N<sub>2</sub> Separation through Nanoporous Graphene from Molecular Dynamics. *Nanoscale* 2013, 5, 9984-9987.
14. Drahushuk, L. W.; Strano, M. S. Mechanisms of Gas Permeation through Single Layer Graphene Membranes. *Langmuir* 2012, 28, 16671-16678.
15. Sun, C.; Boutilier, M. S. H.; Au, H.; Poesio, P.; Bai, B.; Karnik, R.; Hadjiconstantinou, N. G. Mechanisms of Molecular Permeation through Nanoporous Graphene Membranes. *Langmuir* 2013, 30, 675-682.
16. Liu, H.; Dai, S.; Jiang, D.-e. Permeance of H<sub>2</sub> through Porous Graphene from Molecular Dynamics. *Solid State Communications* 2013, 175-176, 101-105.
17. Blankenburg, S.; Bieri, M.; Fasel, R.; Müllen, K.; Pignedoli, C. a.; Passerone, D. Porous graphene as an atmospheric nanofilter. *Small (Weinheim an der Bergstrasse, Germany)* 2010, 6, 2266-71.
18. Jiang, D.-e.; Cooper, V. R.; Dai, S. Porous graphene as the ultimate membrane for gas separation. *Nano letters* 2009, 9, 4019-24.



19. Liu, H.; Chen, Z.; Dai, S.; Jiang, D.-e. Selectivity Trend of Gas Separation through Nanoporous Graphene. *Journal of Solid State Chemistry* 2015, 224, 2-6.
20. Koenig, S. P.; Boddeti, N. G.; Dunn, M. L.; Bunch, J. S. Ultrastrong adhesion of graphene membranes. *Nat Nano* 2011, 6, 543-546.
21. Lei, G.; Liu, C.; Xie, H.; Song, F. Separation of the Hydrogen Sulfide and Methane Mixture by the Porous Graphene Membrane: Effect of the Charges. *Chemical Physics Letters* 2014, 599, 127-132.
22. Tao, Y.; Xue, Q.; Liu, Z.; Shan, M.; Ling, C.; Wu, T.; Li, X. Tunable Hydrogen Separation in Porous Graphene Membrane: First-Principle and Molecular Dynamic Simulation. *ACS Applied Materials & Interfaces* 2014, 6, 8048-8058.
23. Li, Y.; Zhou, Z.; Shen, P.; Chen, Z. Two-dimensional polyphenylene: experimentally available porous graphene as a hydrogen purification membrane. *Chemical communications (Cambridge, England)* 2010, 46, 3672-4.
24. Cohen-Tanugi, D.; Grossman, J. C. Water desalination across nanoporous graphene. *Nano letters* 2012, 12, 3602-8.
25. Konatham, D.; Yu, J.; Ho, T. A.; Striolo, A. Simulation Insights for Graphene-Based Water Desalination Membranes. *Langmuir* 2013, 29, 11884-11897.
26. Cohen-Tanugi, D.; Grossman, J. C. Water Permeability of Nanoporous Graphene at Realistic Pressures for Reverse Osmosis Desalination. *Journal of Chemical Physics* 2014, 141, -.
27. Fileti, E. E.; Dalpian, G. M.; Rivelino, R. Liquid Separation by a Graphene Membrane. *Journal of Applied Physics* 2010, 108, 113527.

28. Hu, G.; Mao, M.; Ghosal, S. Ion transport through a graphene nanopore. *Nanotechnology* 2012, 23, 395501.
29. Sint, K.; Wang, B.; Král, P. Selective Ion Passage through Functionalized Graphene Nanopores. *Journal of the American Chemical Society* 2008, 130, 16448-16449.
30. Qin, X.; Meng, Q.; Feng, Y.; Gao, Y. Graphene with line defect as a membrane for gas separation: Design via a first-principles modeling. *Surface Science* 2013, 607, 153-158.
31. Robeson, L. M. Correlation of separation factor versus permeability for polymeric membranes. *Journal of Membrane Science* 1991, 62, 165-185.
32. Koenig, S. P.; Wang, L.; Pellegrino, J.; Bunch, J. S. Selective molecular sieving through porous graphene. *Nat Nano* 2012, 7, 728-732.
33. Sun, C.; Bai, B. Fast mass transport across two-dimensional graphene nanopores: Nonlinear pressure-dependent gas permeation flux. *Chemical Engineering Science* 2017, 165, 186-191.
34. Sun, C.; Wen, B.; Bai, B. Application of nanoporous graphene membranes in natural gas processing: Molecular simulations of CH<sub>4</sub>/CO<sub>2</sub>, CH<sub>4</sub>/H<sub>2</sub>S and CH<sub>4</sub>/N<sub>2</sub> separation. *Chemical Engineering Science* 2015, 138, 616-621.
35. Cabrales-Navarro, F. A.; Gómez-Ballesteros, J. L.; Balbuena, P. B. Molecular dynamics simulations of metal-organic frameworks as membranes for gas mixtures separation. *Journal of Membrane Science* 2013, 428, 241-250.

36. Venna, S. R.; Carreon, M. A. Highly Permeable Zeolite Imidazolate Framework-8 Membranes for CO<sub>2</sub>/CH<sub>4</sub> Separation. *Journal of the American Chemical Society* 2010, 132, 76-78.
37. Yuan, Z.; Govind Rajan, A.; Misra, R. P.; Drahushuk, L. W.; Agrawal, K. V.; Strano, M. S.; Blankschtein, D. Mechanism and Prediction of Gas Permeation through Sub-Nanometer Graphene Pores: Comparison of Theory and Simulation. *ACS Nano* 2017, 11, 7974-7987.
38. Garaj, S.; Hubbard, W.; Reina, A.; Kong, J.; Branton, D.; Golovchenko, J. A. Graphene as a subnanometre trans-electrode membrane. *Nature* 2010, 467, 190-3.
39. Merchant, C. A.; Healy, K.; Wanunu, M.; Ray, V.; Peterman, N.; Bartel, J.; Fischbein, M. D.; Venta, K.; Luo, Z.; Johnson, A. T. C.; Drndić, M. DNA Translocation through Graphene Nanopores. *Nano letters* 2010, 10, 2915-2921.
40. Schneider, G. F.; Kowalczyk, S. W.; Calado, V. E.; Pandraud, G.; Zandbergen, H. W.; Vandersypen, L. M. K.; Dekker, C. DNA translocation through graphene nanopores. *Nano letters* 2010, 10, 3163-7.
41. Hankel, M.; Jiao, Y.; Du, A.; Gray, S. K.; Smith, S. C. Asymmetrically Decorated, Doped Porous Graphene As an Effective Membrane for Hydrogen Isotope Separation. *The Journal of Physical Chemistry C* 2012, 116, 6672-6676.
42. Hauser, A. W.; Schrier, J.; Schwerdtfeger, P. Helium Tunneling through Nitrogen-Functionalized Graphene Pores: Pressure- and Temperature-Driven Approaches to Isotope Separation. *The Journal of Physical Chemistry C* 2012, 116, 10819-10827.
43. Hauser, A. W.; Schwerdtfeger, P. Nanoporous Graphene Membranes for Efficient <sup>3</sup>He/ <sup>4</sup>He Separation. *The Journal of Physical Chemistry Letters* 2012, 3, 209-213.

44. Schrier, J.; McClain, J. Thermally-driven isotope separation across nanoporous graphene. *Chemical Physics Letters* 2012, 521, 118-124.
45. Wang, L.; Drahushuk, L. W.; Cantley, L.; Koenig, S. P.; Liu, X.; Pellegrino, J.; Strano, M. S.; Bunch, J. S. Molecular Valves for Controlling Gas Phase Transport Made from Discrete ångström-sized Pores in Graphene. *Nature Nanotechnology* 2015, 10, 785-790.
46. O'Hern, S. C.; Stewart, C. A.; Boutilier, M. S. H.; Idrobo, J.-C.; Bhaviripudi, S.; Das, S. K.; Kong, J.; Laoui, T.; Atieh, M.; Karnik, R. Selective Molecular Transport through Intrinsic Defects in a Single Layer of CVD Graphene. *ACS Nano* 2012, 6, 10130-10138.
47. Boutilier, M. S. H.; Sun, C.; O'Hern, S. C.; Au, H.; Hadjiconstantinou, N. G.; Karnik, R. Implications of Permeation through Intrinsic Defects in Graphene on the Design of Defect-Tolerant Membranes for Gas Separation. *ACS Nano* 2014, 8, 841-849.
48. Walker, M. I.; Weatherup, R. S.; Bell, N. A. W.; Hofmann, S.; Keyser, U. F. Free-standing Graphene Membranes on Glass Nanopores for Ionic Current Measurements. *Applied Physics Letters* 2015, 106, 023119.
49. Celebi, K.; Buchheim, J.; Wyss, R. M.; Droudian, A.; Gasser, P.; Shorubalko, I.; Kye, J.-I.; Lee, C.; Park, H. G. Ultimate Permeation Across Atomically Thin Porous Graphene. *Science* 2014, 344, 289-292.
50. Boutilier, M. S. H.; Jang, D.; Idrobo, J.-C.; Kidambi, P. R.; Hadjiconstantinou, N. G.; Karnik, R. Molecular Sieving Across Centimeter-Scale Single-Layer Nanoporous Graphene Membranes. *ACS Nano* 2017, 11, 5726-5736.

51. Chen, Y. Nanofabrication by electron beam lithography and its applications: A review. *Microelectronic Engineering* 2015, 135, 57-72.
52. Han, M. Y.; Özyilmaz, B.; Zhang, Y.; Kim, P. Energy Band-Gap Engineering of Graphene Nanoribbons. *Physical Review Letters* 2007, 98, 206805.
53. Sprinkle, M.; Ruan, M.; Hu, Y.; Hankinson, J.; Rubio-Roy, M.; Zhang, B.; Wu, X.; Berger, C.; de Heer, W. a. Scalable templated growth of graphene nanoribbons on SiC. *Nature Nanotechnology* 2010, 5, 727-731.
54. Jiao, L.; Zhang, L.; Wang, X.; Diankov, G.; Dai, H. Narrow graphene nanoribbons from carbon nanotubes. *Nature* 2009, 458, 877-880.
55. Salaita, K.; Wang, Y.; Mirkin, C. A. Applications of dip-pen nanolithography. *Nat Nano* 2007, 2, 145-155.
56. Sakellari, I.; Kabouraki, E.; Gray, D.; Purlys, V.; Fotakis, C.; Pikulin, A.; Bityurin, N.; Vamvakaki, M.; Farsari, M. Diffusion-Assisted High-Resolution Direct Femtosecond Laser Writing. *ACS Nano* 2012, 6, 2302-2311.
57. Voigt, J.; Shi, F.; Edinger, K.; Güthner, P.; Rangelow, I. W. Nanofabrication with scanning nanonozzle 'Nanojet'. *Microelectronic Engineering* 2001, 57-58, 1035-1042.
58. Goto, M.; Zhigilei, L. V.; Hobbey, J.; Kishimoto, M.; Garrison, B. J.; Fukumura, H. Laser expulsion of an organic molecular nanojet from a spatially confined domain. *Journal of Applied Physics* 2001, 90, 4755-4760.
59. Knudsen, M. The molecular current of gases through openings and the effusion. *Ann. Phys., Lpz.* 1909, 28, 75-130.
60. Satterfield, C. N.; Colton, C. K.; Pitcher, W. H. Restricted diffusion in liquids within fine pores. *AIChE Journal* 1973, 19, 628-635.

61. Chantong, A.; Massoth, F. E. Restrictive diffusion in aluminas. *AIChE Journal* 1983, 29, 725-731.
62. Freeman, D. L. The influence of diffusion on surface reaction kinetics. *The Journal of Chemical Physics* 1983, 78, 6002-6002.
63. Schrier, J. Fluorinated and nanoporous graphene materials as sorbents for gas separations. *ACS applied materials & interfaces* 2011, 3, 4451-8.
64. Kolasinski, K. W. *Surface science : foundations of catalysis and nanoscience*. Wiley: Chichester, England; Hoboken, NJ, 2008.
65. Russo, C. J.; Golovchenko, J. A. Atom-by-atom nucleation and growth of graphene nanopores. *Proceedings of the National Academy of Sciences of the United States of America* 2012, 109, 5953-7.
66. Drahushuk, L. W.; Wang, L.; Koenig, S. P.; Bunch, J. S.; Strano, M. S. Analysis of Time-Varying, Stochastic Gas Transport through Graphene Membranes. *ACS Nano* 2015, 10, 786-795.
67. Bunch, J. S. *Mechanical and Electrical Properties of Graphene Sheets*. Cornell University, Ithaca, 2008.
68. McKinney, S. A.; Joo, C.; Ha, T. Analysis of Single-Molecule FRET Trajectories Using Hidden Markov Modeling. *Biophysical Journal* 2006, 91, 1941-1951.
69. Reid, R. C.; Prausnitz, J. M.; Poling, B. E. *The Properties of Gases and Liquids*. McGraw-Hill: New York, 1987.
70. Steele, W. A. *The Interaction of Gases with Solid Surfaces*. Pergamon Press: Oxford, U.K., 1974.

71. Cembran, A.; Bernardi, F.; Garavelli, M.; Gagliardi, L.; Orlandi, G. On the Mechanism of the cis–trans Isomerization in the Lowest Electronic States of Azobenzene: S<sub>0</sub>, S<sub>1</sub>, and T<sub>1</sub>. *Journal of the American Chemical Society* 2004, 126, 3234-3243.
72. Son, Y.-W.; Cohen, M. L.; Louie, S. G. Energy Gaps in Graphene Nanoribbons. *Physical Review Letters* 2006, 97, 216803.
73. Chen, Y.-C.; de Oteyza, D. G.; Pedramrazi, Z.; Chen, C.; Fischer, F. R.; Crommie, M. F. Tuning the Band Gap of Graphene Nanoribbons Synthesized from Molecular Precursors. *ACS Nano* 2013, 7, 6123-6128.
74. Jacobberger, R. M.; Kiraly, B.; Fortin-Deschenes, M.; Levesque, P. L.; McElhinny, K. M.; Brady, G. J.; Rojas Delgado, R.; Singha Roy, S.; Mannix, A.; Lagally, M. G.; Evans, P. G.; Desjardins, P.; Martel, R.; Hersam, M. C.; Guisinger, N. P.; Arnold, M. S. Direct oriented growth of armchair graphene nanoribbons on germanium. *Nat Commun* 2015, 6.
75. Li, X.; Magnuson, C. W.; Venugopal, A.; Tromp, R. M.; Hannon, J. B.; Vogel, E. M.; Colombo, L.; Ruoff, R. S. Large-Area Graphene Single Crystals Grown by Low-Pressure Chemical Vapor Deposition of Methane on Copper. *Journal of the American Chemical Society* 2011, 133, 2816-2819.
76. Dunn, R. C. Near-Field Scanning Optical Microscopy. *Chemical Reviews* 1999, 99, 2891-2928.
77. Marrero, T. R.; Mason, E. A. Gaseous Diffusion Coefficients. *Journal of Physical and Chemical Reference Data* 1972, 1, 3-118.

78. Agrawal, K. V.; Benck, J. D.; Yuan, Z.; Misra, R. P.; Govind Rajan, A.; Eatmon, Y.; Kale, S.; Chu, X. S.; Li, D. O.; Gong, C.; Warner, J.; Wang, Q. H.; Blankschtein, D.; Strano, M. S. Fabrication, Pressure Testing, and Nanopore Formation of Single-Layer Graphene Membranes. *The Journal of Physical Chemistry C* 2017, 121, 14312-14321.
79. Michael, S. H. B.; Nicolas, G. H.; Rohit, K. Knudsen effusion through polymer-coated three-layer porous graphene membranes. *Nanotechnology* 2017, 28, 184003.
80. Lee, C. Y.; Choi, W.; Han, J.-H.; Strano, M. S. Coherence Resonance in a Single-Walled Carbon Nanotube Ion Channel. *Science* 2010, 329, 1320.